Hindawi
International Journal of Energy Research
Volume 2024, Article ID 7844084, 22 pages
https://doi.org/10.1155/2024/7844084

Research Article

Optimal Adaptive Fractional Order Integral Sliding Mode Controller-Energy Management Strategy for Electric Vehicles Based on Bald Eagle Search Algorithm

Houssam Eddine Ghadbane,[1] Said Barkat,[2] Azeddine Houari,[3] Ali Djerioui,[2] Hegazy Rezk,[4] and Mohamed Louzazni[5]

[1]*Laboratoire de Génie Électrique de Guelma (LGEG), Département de Génie Electrotechnique et Automatique, Université 8 Mai 1945, B.P.401, Guelma 24000, Algeria*
[2]*University of M'sila, Electrical Engineering Laboratory, Electrical Engineering Department, Algeria*
[3]*Institut de Recherche en Énergie Électrique de Nantes Atlantique, IREENA, Nantes Université, 44600 Saint-Nazaire, France*
[4]*Department of Electrical Engineering, College of Engineering in Wadi Alddawasir, Prince Sattam bin Abdulaziz University, Saudi Arabia*
[5]*Science Engineer Laboratory for Energy, National School of Applied Sciences, Chouaib Doukkali University of El Jadida, El Jadida, Morocco*

Correspondence should be addressed to Mohamed Louzazni; louzazni.m@ucd.ac.ma

Received 25 July 2023; Revised 2 October 2023; Accepted 15 December 2023; Published 20 February 2024

Academic Editor: R. Palanisamy

This research presents an optimal energy management system (EMS) for a lithium-ion battery-supercapacitor hybrid storage system used to power an electric vehicle. The storage systems are connected in parallel to the DC bus by bidirectional DC-DC converters and feed a synchronous reluctance motor through an inverter. The proposed energy management strategy is built on the idea to take full benefits of two combined methods: the bald eagle search algorithm and fractional order integral sliding mode control. To evaluate the effectiveness of the suggested optimal energy management strategy, an urban dynamometer driving schedule (UDDS) driving cycle is considered. The obtained results are compared to a classical fractional order integral sliding mode control-based energy management strategy in terms of voltage ripples, overshoots, and battery final state of charge. The ultimate results approve the ability of the proposed energy management system to enhance the power quality and enhance battery power consumption at the same time. Comprehensive processor-in-the-loop (PIL) cosimulations were conducted on the electric vehicle using the C2000 launchxl-f28379d digital signal processing (DSP) board to assess the practicability and effectiveness of the proposed EMS.

1. Introduction

Currently, the influence of transportation system growth on global warming and climate change is becoming more visible and omnipresent [1–3]. Due to increased passenger number and inland freight volume, European Union (EU) domestic transport emissions increased progressively between 2013 and 2019. As a consequence of a significant decrease in transport activity during the COVID-19 pandemic, emissions declined by 13.6% between 2019 and 2020. In 2021, the economic recovery led to a rise in emissions of 7.7% [4]. Using electric vehicles (EVs) as a means of electrifying transportation seems to be the most effective option for reducing the amount of carbon dioxide produced by transportation [5, 6]. EVs powered by hybrid power systems (HPSs) are gaining popularity because of the enhanced power quality, durability, and reliable performance that these systems provide [7–9]. Battery-supercapacitor hybrid

power systems have garnered increasing attention owing to their enhanced performance and ease of control. While lithium batteries possess a notably high-energy density, they lack a correspondingly high-power density, a shortcoming that supercapacitors excel in. Therefore, combining these two technologies through hybridization proves to be a viable strategy to enhance the longevity of both components and optimize overall system performance. This is particularly valuable when considering the state of charge and temperature conditions of energy storage elements. One illustrative example of this synergy is the utilization of supercapacitors to handle sudden load fluctuations. Furthermore, it is worth noting that high-frequency disturbances can detrimentally impact the lifespan of batteries. However, this issue can be mitigated by incorporating supercapacitors into the system due to their distinctive characteristics [10].

Typical HPS includes a battery as the main source and supercapacitor (SC) as the secondary source. Because it has a high-energy density, the battery is the motor primary power source. At the same time, the SC, which has a high-power density, contributes to improving the power quality by supplying rapid changes in the motor output power. In the EV, the traction electric machine has the same importance as HPS. Many electric machines are used in traction applications including interior permanent magnet synchronous machine, induction machine, and switched reluctance machine. Nowadays, synchronous reluctance motor (SynRM) has become more and more popular in electric vehicle applications [11]. This is due to its greater efficiency, simplicity and reliability, cost-effectiveness, cooling and thermal management, application flexibility, and less weight, and it is more affordable [11–17]. In addition, SynRM is capable of delivering 34% more torque than traditional machines, which makes it appropriate for use in the electric vehicle sector [18].

In the EV, it is necessary to design an adequate energy management strategy in charge of distributing power across the HPS sources, considering many different limits that must be met to improve performance and increase battery life. Nevertheless, the effectiveness of the selected EMS is the primary concern here. In order to achieve this goal, several EMSs have been published in the research literature. In general, the EMSs may be broken down into optimization, rule-based, and learning-based techniques, as stated in [19–23]. Approaches based on optimization make use of the tools that optimization theory is involved in order to solve the problem at hand. The purpose is to achieve an optimal distribution of load power throughout the battery-supercapacitor storage system in order to maximize the life expectancies of each component. Methods that are focused on optimization may be categorized as either offline (on a global scale) or online (on a real-time scale). Offline optimization EMS consists of finding an optimum control solution for a problem over a condition that has already been determined, like a speed profile. There are two methods: direct methods include approaches like disciplined optimum control; indirect methods include approaches like the calculus of variations [20], Pontryagin's maximum principle (PMP) [24], Pontryagin's minimum principle [25, 26], stochastic dynamic programming (SDP) [27], and dynamic programming (DP) [21, 28]. One of the real-time uses of online optimization is figuring out the best way to distribute energy in a hybrid system by utilizing the data that has been specified. The cost function may take into account the system current status in addition to the running costs and emissions. The model predictive control (MPC) [29, 30], the equivalent consumption minimization strategy (ECMS) [31], and the external energy maximization strategy (EEMS) [32] are all examples of strategies that fall within this category. Learning-based techniques, as an area of artificial intelligence, recently leverage developments in machine learning, notably reinforcement learning (RL) [33, 34] and deep learning (DL) [35, 36]. They have shown their efficacy in various fields, most notably image categorization, which has led to the broad implementation of their use in energy management [37–41]. The databases are required to train a model; however, they are not yet accessible. This is a challenge since there has not been nearly enough study done on the new topic. They provide no assurances that they will work with data beyond the training provided. Rule-based methods are constructed on the foundation of a series of "IF-THEN" scenarios. This category may be further broken down into two different subcategories: deterministic strategies, such as the state machine control (SMC) approach [42], and intelligent methods, such as the fuzzy logic-based EMS [43, 44]. Creating these strategies' responsibilities requires the designer's expertise, which is not always accessible. This is the primary drawback of these methods. They also suffer from problems related to the abrupt transitions between the various operating modes, which presents a real challenge for conventional controllers to keep the desired power quality and system stability. Numerous linear and nonlinear controllers have been proposed to control HPS, such as proportional-integral (PI) control [45], passivity control [46–48], flatness-based control [49, 50], backstepping-based control [51], sliding mode control [52, 53], adaptive sliding mode control strategy [54], sliding mode state and perturbation observer (SMSPO) [55, 56], H-infinity control [57], active disturbance rejection control [58, 59], and fractional order sliding mode control (FOSMC) [60, 61]. Although the previously mentioned control methods are extremely useful to the readers, none of them have the benefits of a control approach with optimization-based technique.

This paper suggested an optimal fractional order integral sliding mode control (FO-ISMC) strategy for managing the power flow in an electric vehicle power system. For this, bald eagle search (BES) optimization algorithm is adopted to better identify dynamically the FO-ISMC parameters, with a view to enhancing the HPS control and management. In this perspective, the present paper seeks to achieve the following main objectives:

(i) Enhance the power system overall efficiency

(ii) Ensuring the effective utilization of the power flows between the battery and the SC while adhering to the constraints imposed by the state of charge (SoC)

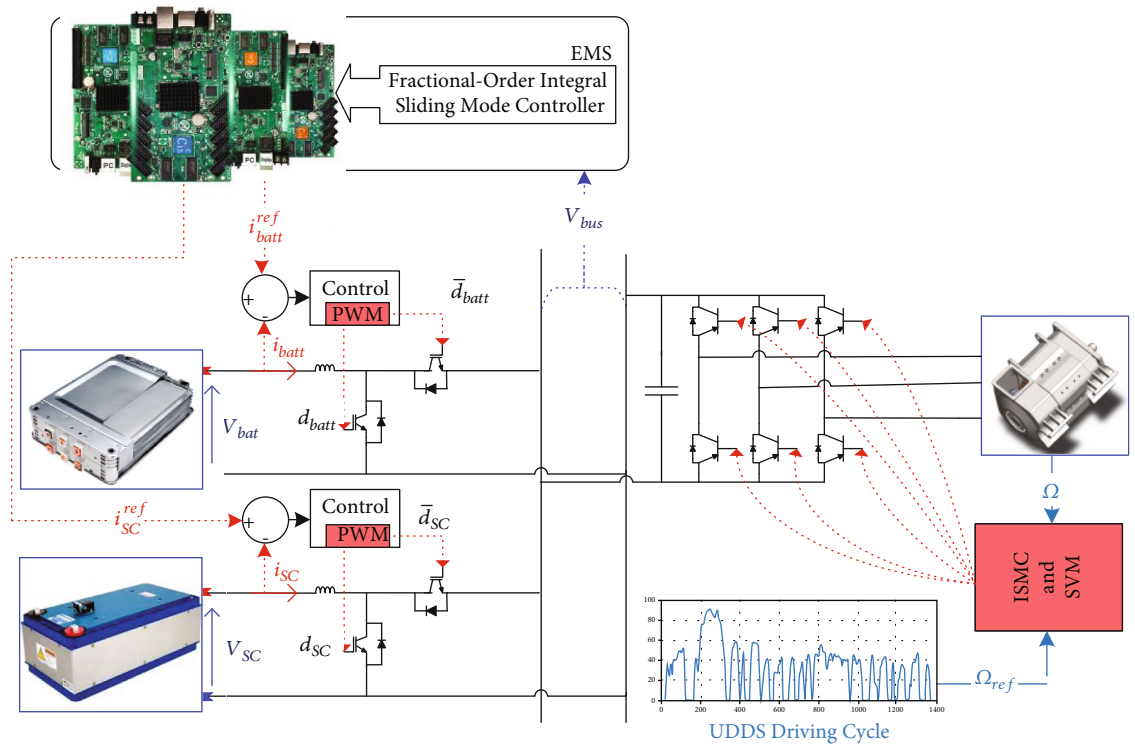

Figure 1: Schematic structure of the proposed electrical vehicle.

(iii) Maintaining voltage stability on the DC bus

(iv) Employing a variety of strategies in concert with one another to get optimal results

The rest of the study is summarized as follows: Section 2 describes and models the HPS under consideration. The control techniques for the traction chain are detailed in Section 3. Section 4 details the suggested optimum adaptive FO-ISMC-based EMS. Section 5 presents the simulation and cosimulation results and their interpretations. In the sixth section of this study report, some conclusions are presented.

2. Power System Configuration and Modeling

The selected electric vehicle has both a Li-ion battery and a supercapacitor as energy storage systems, two bidirectional boost converters (BBC) connected to the same DC bus; one of these converters manages the flow of power to and from the battery, while the other converter controls the flow of power to and from the SC. Additionally, a synchronous reluctance motor is supplied directly from the inverter, as shown in Figure 1.

2.1. BBC Modeling. The DC-DC converters provide a large amount of flexibility by either providing power to the DC bus to enhance the voltage level (boost behavior) or receiving power from the DC bus to lower the voltage level (buck behavior). The following average model for the two BBCs is taken into account in this study:

$$\begin{cases} L_{\text{bat}} \dfrac{di_{\text{bat}}}{dt} = V_{\text{bat}} - V_{\text{bus}} d_{\text{batt}} - r_{\text{Bat}} i_{\text{batt}}, \\ L_{\text{sc}} \dfrac{di_{\text{sc}}}{dt} = V_{\text{SC}} - V_{\text{bus}} d_{\text{sc}} - r_{\text{SC}} i_{\text{SC}}, \\ c_{\text{bus}} \dfrac{dV_{\text{bus}}}{dt} = d_{\text{batt}} i_{\text{bat}} + d_{\text{sc}} i_{\text{SC}} - i_{\text{Load}}, \end{cases} \tag{1}$$

where V_{SC} is the supercapacitor voltage, V_{bus} is the DC bus voltage, r_{SC} and r_{batt} denote the internal converter resistors, L_{SC} and L_{batt} are the DC-DC converter inductors, d_{SC} and d_{batt} are the converter duty cycle ratios, C_{bus} is the DC bus capacitance, and i_{SC}, i_{batt}, and i_{Load} are the supercapacitor, battery, and load currents, respectively.

2.2. SynRM and EV Dynamic Modeling. There are a few different primary rotor architectures that can be found in SynRM at present. These include the solid rotor, the flux barrier rotor, the axially laminated rotor, and the magnet-assisted rotor. Those structures with flux barriers are the ones that are most suited for traction applications because they satisfy the criteria for performance, robustness, cost, and manufacture [12]. The following equation

presents the electromechanical model of SynRM when seen in the $(d\text{-}q)$ frame:

$$\frac{d}{dt}\begin{bmatrix} i_{\mathrm{sd}} \\ i_{\mathrm{sq}} \\ \omega_{\mathrm{m}} \\ \theta \end{bmatrix} = \begin{bmatrix} \dfrac{-R_{\mathrm{s}}}{L_d} i_{\mathrm{sd}} + \dfrac{pL_q}{L_d} i_{\mathrm{sq}} \omega_{\mathrm{m}} \\ \dfrac{-R_{\mathrm{s}}}{L_q} i_{\mathrm{sq}} - \dfrac{pL_d}{L_q} i_{\mathrm{sd}} \omega_{\mathrm{m}} \\ \dfrac{1}{J}\left(\dfrac{3}{2} p\left(L_d - L_q\right) i_{\mathrm{sd}} i_{\mathrm{sq}} - f_{\mathrm{r}} \omega_{\mathrm{m}} - \dfrac{T_{\mathrm{L}}}{J}\right) \\ p\omega_{\mathrm{m}} \end{bmatrix} + \begin{bmatrix} \dfrac{1}{L_d} & 0 \\ 0 & \dfrac{1}{L_q} \\ 0 & 0 \\ 0 & 0 \end{bmatrix} \begin{bmatrix} v_{\mathrm{sd}} \\ v_{\mathrm{sq}} \end{bmatrix}, \tag{2}$$

where v_{sq} and v_{sd} are the quadrature and direct axis stator voltages, respectively. i_{sq} and i_{sd} represent their corresponding currents. The L_d and L_q are the d-q magnetizing inductances. ω_{m} represents the mechanical rotation speed, R_{s} represents the stator resistance, p denotes the number of pair poles, T_{L} is the load torque, and f_{r} and J represent the viscous friction coefficient and inertia moment, respectively.

The equation representing the dynamics of SynRM is formulated as follows:

$$T_{\mathrm{e}} - T_{\mathrm{Load}} = J_{\mathrm{ve}} \frac{d\Omega}{dt}. \tag{3}$$

The load torque is provided by

$$T_{Load} = \frac{T_{Lwheel}}{i} = \frac{r}{i}\left[\left(m_v\, g\, \mu\, sign(v)\right) + \left(0.5\, \gamma\, C_d\, A_f\, (v \pm v_w)^2\right) \pm \left(m_v\, g\ \sin\ \alpha\right) \pm \left(k_m\, m_v \frac{dv}{dt}\right)\right], \tag{4}$$

where T_{Lwheel}, i, and r represent the load torque on the wheels, the transmission ratio, and the wheel radius, respectively; v and v_{w} are the vehicle and wind speed, respectively; α represents the angle of the slope; m_{v} is the vehicle mass; μ, k_{m}, and C_{d} are the tire rolling resistance, the rotational inertia, and aerodynamic drag coefficient, respectively; γ and A_f represent the air density and the frontal vehicle area, respectively; and g represents the earth's gravity.

The SynRM and vehicle parameters are listed in the appendix, respectively.

Having discussed the fundamental elements of power system configuration and modeling, we can now proceed to examine efficient system control strategies.

3. System Control Strategies

The proposed control systems center around two main objectives. The first one consists of the fractional order integral sliding mode controller (FO-ISMC), which is applied to the bidirectional DC-DC converter. The second one resides in the integral sliding mode control (ISMC) of the SynRM, aiming to improve the performance of the drive system.

3.1. BBC FO-ISMC Design

3.1.1. Explanations of Fractional Derivatives and Integrals. In the field of applied mathematics, particularly in areas where integrals and differentiators are used, the fractional order calculus has a number of applications that are both intriguing and useful. The calculus of the fractional order is used to transform the integral integrators and differentiators of any complex or real order into their corresponding fractional counterparts. The fractional order operator is represented by the symbol ${}_cD_t^{\beta}$, and its definition may be written down in this manner [62]:

$${}_cD_t^{\beta} \cong D^{\beta} = \begin{cases} \dfrac{d^{\beta}}{dt^{\beta}} & , \mathrm{Re}\ (\beta) > 0, \\ 1 & , \mathrm{Re}\ (\beta) = 0, \\ \displaystyle\int_a^t (d\tau)^{-\beta} & , \mathrm{Re}\ (\beta) < 0. \end{cases} \tag{5}$$

In this expression, c and t stand for the operational limits, β stands for the order of the fractional operator, and Re denotes the real component of beta.

The fractional differential and integration that Riemann and Liouville developed may be specifically defined [62].

$$\begin{aligned} {}_cD_t^{\beta} f(t) &= \frac{d^{\beta}}{dt^{\beta}} f(t) = \frac{1}{\Gamma(n-\beta) dt^n} \int_{\beta}^{t} \frac{f(\tau)}{(t-\tau)^{\beta-n+1}} d\tau, \\ {}_cD_t^{-\beta} f(t) &= I^{\beta} f(t) = \frac{1}{\Gamma(\beta)} \int_{\beta}^{t} \frac{f(\tau)}{(t-\tau)^{1-\beta}} d\tau. \end{aligned} \tag{6}$$

The Euler gamma function, denoted by $\Gamma(.)$, has the following definition:

$$\Gamma(x) = \int_0^{\infty} e^{-t} t^{(x-1)} dt, x > 0. \tag{7}$$

For defining the fractional order integrator and derivative, the Grunwald-Letnikov approach provides the following formula:

$${}_c^{\mathrm{GL}}D_t^{-\beta} f(t) = \lim_{h \longrightarrow 0} \frac{1}{h^{\beta}} \sum_{j=0}^{[(t-\beta)/h]} (-1)^j \binom{\beta}{j} f(t - jh). \tag{8}$$

DC-DC converters are controlled by a cascade of inner FO-ISMC current control loops and an outer voltage FO-ISMC controller.

3.1.2. FO-ISMC-Based DC Bus Voltage Control. The following voltage fractional order integral sliding surface (FO-ISS) (S_{v}) is selected for the DC bus voltage control:

$$S_{\mathrm{v}} = k_{\mathrm{v1}} \int \dot{e}_{\mathrm{vbus}} + k_{\mathrm{v2}} D^{-\beta} e_{\mathrm{vbus}}, \tag{9}$$

where the k_{v1} and k_{v2} and $D^{-\beta}$ and β are the voltage FO-ISS coefficients and the voltage integral fractional order operator and fractional order, respectively, and e_{vbus} is the DC bus voltage error, expressed as follows:

$$e_{vbus} = V^*_{bus} - V_{bus}. \tag{10}$$

The fractional derivative of sliding surface produces the following equation:

$$D^{\beta} S_v = k_{v1} D^{\beta-1} \dot{e}_{vbus} + k_{v2} e_{vbus} = -\lambda_i \mathrm{Sign}(S_v). \tag{11}$$

The current i^*_c may be expressed as

$$i^*_c = \frac{c_{bus}}{k_{v1}} D^{1-\beta}[\lambda_v \mathrm{Sign}(S_v) + k_{v2}(V^*_{bus} - V_{bus})] + c_{bus}\frac{dV^*_{bus}}{dt}. \tag{12}$$

The command is expressed as follows:

$$i^*_{dc} = \frac{c_{bus}}{k_{v1}} D^{1-\beta}[\lambda_v \mathrm{Sign}(S_v) + k_{v2}(V^*_{bus} - V_{bus})] + c_{bus}\frac{dV^*_{bus}}{dt} + i^*_{Load}. \tag{13}$$

3.1.3. FO-ISMC-Based Battery/Supercapacitor Current Control. The FO-ISS $(S_{i(bat,SC)})$ of battery/supercapacitor current controllers are defined as

$$\begin{aligned} S_{ibat} &= k_{i1}\int \dot{e}_{ibat} + k_{i2} D^{-\delta bat} e_{ibat}, \\ S_{isc} &= k_{i3}\int \dot{e}_{isc} + k_{i4} D^{-\delta sc} e_{isc}, \end{aligned} \tag{14}$$

with k_{i1}, k_{i2}, k_{i3}, and k_{i4} and δbat and δsc are the coefficients of the battery/supercapacitor current FO-ISS and the fractional orders and e_{bat} and e_{sc} are the battery/supercapacitor current errors defined as follows:

$$e_{bat} = i^*_{bat} - i_{bat}, \tag{15}$$

$$e_{sc} = (i^*_{sc} - i_h) - i_{sc}, \tag{16}$$

where i_h is the harmonic current and i^*_{bat}, i^*_{sc} are the battery/supercapacitor reference currents.

The $S_{i(bat,SC)}$ fractional order derivative yields the following expressions:

$$D^{\delta bat} S_{ibat} = k_{i1} D^{\delta bat-1} \dot{e}_{ibat} + k_{i2} e_{ibat} = -\lambda_{ibat} \mathrm{Sign}(S_{ibat}), \tag{17}$$

$$D^{\delta sc} S_{isc} = k_{i3} D^{\delta sc-1} \dot{e}_{isc} + k_{i4} e_{ibat} = -\lambda_{isc} \mathrm{Sign}(S_{isc}). \tag{18}$$

The expressions of the commands $u_{bat,SC}$ are given as follows:

$$u_{bat} = \frac{L_{bat}}{k_{i1} V_{bus}} D^{1-\delta bat}\left[\lambda_{ibat}\mathrm{Sign}(S_{ibat}) + k_{i2} e_{ibat} + k_{i1}\frac{di^*_{bat}}{dt}\right] - \frac{V_{bat} - r_{bat} i_{bat}}{V_{bus}}, \tag{19}$$

$$u_{sc} = \frac{L_{sc}}{k_{i3} V_{bus}} D^{1-\delta sc}\left[\lambda_{isc}\mathrm{Sign}(S_{isc}) + k_{i4} e_{isc} + k_{i3}\frac{di^*_{sc}}{dt}\right] - \frac{V_{bat} - r_{sc} i_{sc}}{V_{bus}}, \tag{20}$$

where $\lambda_v, \lambda_{i(bat,sc)}$ are positive constants.

3.1.4. Proof of Stability. For the purpose of demonstrating the closed-loop stability of the suggested control strategy, a Lyapunov theorem that was presented by Aghababa is applied [63]. In two separate stages, the robustness of the system as a whole will be shown. In the first phase of the process, the voltage loop is investigated, and then, the current loop is examined. In order to demonstrate the stability, the following theorem will be applied.

The stability of the proposed FO-ISMC, obtained in Eqs. (15), (19), and (20), for the system provided in Eq. (11), is determined by whether the following inequality is correct [18]:

$$\left|\sum_{j=1}^{\infty} \frac{\Gamma(1+\beta)}{\Gamma(1-j+\beta)\Gamma(1+j)} D^j S_v D^{\beta-j} S_v\right| \le \vartheta_1(S_v). \tag{21}$$

Thus, ϑ_1 denotes a positive constant.

(1) Voltage Loop Demonstration. In order to provide proof that the voltage loop is stable, the Lyapunov candidate function has been described as follows:

$$L_V = \frac{1}{2} S_v^2. \tag{22}$$

When D^{β} is applied to equation (21), the following equation is obtained [42]:

$$D^{\beta} L_V = S_v D^{\beta} S_v + \left|\sum_{j=1}^{\infty} \frac{\Gamma(1+\beta)}{\Gamma(1-j+\beta)\Gamma(1+j)} D^j S_v D^{\beta-j} S_v\right|. \tag{23}$$

Combining Equation (23) with Equation (11) and Equation (21) results in a simplification of the expression:

$$D^{\beta} L_V \le S_v\left[k_{v2}(V^*_{bus} - V_{bus}) + k_{v1} D^{\beta-1}\left(\dot{V}^*_{bus} - \frac{i^*_{dc} - i^*_{Load}}{c_{bus}}\right)\right] + \vartheta_1(S_v). \tag{24}$$

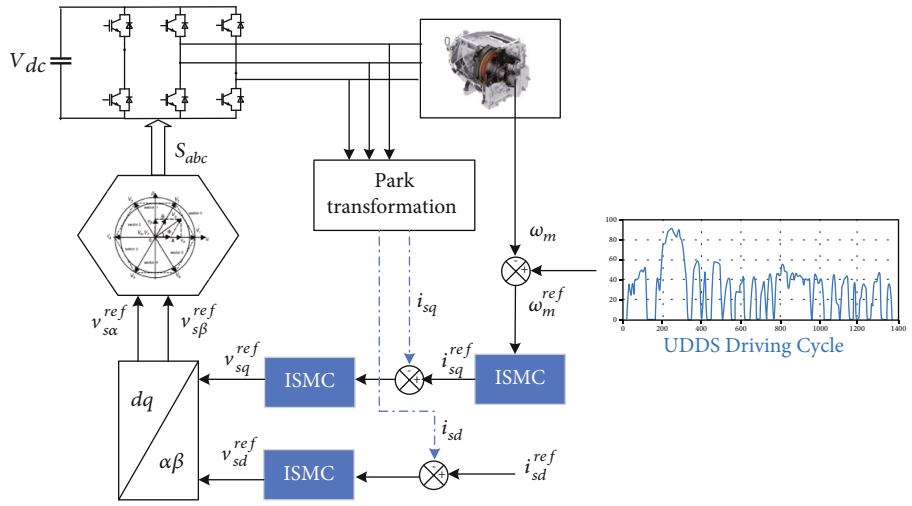

FIGURE 2: Integral sliding mode controller (ISMC) of synchronous reluctance motor schemes.

When Equation (13) and Equation (23) are combined, the following equation may be found:

$$D^{\beta}L_{V} \le S_{v}\left(k_{v2}e_{vbus} + k_{v1}D^{\beta-1}\left\{\frac{dV_{bus}^{*}}{dt} + \frac{i_{Load}^{*}}{c_{bus}} - \frac{1}{k_{v1}}D^{1-\beta}\cdot\left\{\begin{matrix}\lambda_{v}\mathrm{Sign}(S_{v})\\ +k_{v2}e_{vbus}\end{matrix}\right\} - \frac{dV_{bus}^{*}}{dt} - \frac{i_{Load}^{*}}{c_{bus}}\right\}\right) + \vartheta_{1}(S_{v}). \tag{25}$$

The following equation is obtained by further simplifying Eq. (25), which is as follows:

$$D^{\beta}L_{V} \le -\lambda_{v}|S_{v}| + \vartheta_{1}(S_{v}). \tag{26}$$

By allowing $\lambda_{v} > \vartheta_{1}$, it is simple to show that $D^{\beta}L_{V} \le 0$ meets the sliding surface's reaching condition and $S_{v} = 0$.

(2) Current Loop Proof. The following Lyapunov candidate function is utilized to demonstrate the stability of the current loop:

$$L_{Ibat} = \frac{1}{2}S_{ibat}^{2}. \tag{27}$$

When D^{β} is applied to equation (21), the following equation is obtained [42]:

$$D^{\delta bat}L_{V} = S_{Ibat}D^{\delta bat}S_{Ibat} + \left|\sum_{j=1}^{\infty}\frac{\Gamma(1+\beta)}{\Gamma(1-j+\beta)\Gamma(1+j)}D^{j}S_{Ibat}D^{\delta bat-j}S_{Ibat}\right|. \tag{28}$$

Combining Equation (28) with Equation (17) and Equation (21) results in a simplification of the expression:

$$D^{\delta bat}L_{Ibat} \le S_{Ibat}\left[k_{i1}D^{\delta bat-1}\left(\frac{di_{bat}^{*}}{dt} - \frac{1}{L_{bat}}\left(V_{bat} - V_{bus}u_{bat} - r_{bat}i_{bat}\right)\right) + k_{i2}e_{ibat}\right] + \vartheta_{2}(S_{Ibat}). \tag{29}$$

When Equation (19) and Equation (29) are combined, the following equation may be found:

$$D^{\delta bat}L_{Ibat} \le S_{ibat}\left(k_{i2}e_{ibat} + k_{i1}D^{\delta bat-1}\left\{\frac{di_{bat}^{*}}{dt} - \frac{V_{bat}}{L_{bat}} - \frac{1}{k_{i1}}D^{1-\delta bat}\cdot\left\{\begin{matrix}\lambda_{ibat}\mathrm{Sign}(S_{ibat})\\ +k_{i2}e_{ibat}\\ +k_{i1}\dfrac{di_{bat}^{*}}{dt}\end{matrix}\right\} + \frac{V_{bat} + r_{bat}i_{bat}}{L_{bat}} - \frac{r_{bat}i_{bat}}{L_{bat}}\right\}\right) + \vartheta_{2}(S_{ibat}). \tag{30}$$

The following equation is obtained by further simplifying Eq. (30), which is as follows:

$$D^{\delta bat}L_{Ibat} \le -\lambda_{ibat}|S_{ibat}| + \vartheta_{2}(S_{ibat}). \tag{31}$$

By allowing $\lambda_{ibat} > \vartheta_{2}$, it is simple to show that $D^{\delta bat}L_{Ibat} \le 0$ meets the sliding surface's reaching condition and $S_{ibat} = 0$.

3.2. SynRM Integral Sliding Mode Control Approach. Figure 2 is a representation of the three control loops that are a part of the SynRM integral sliding mode control. These

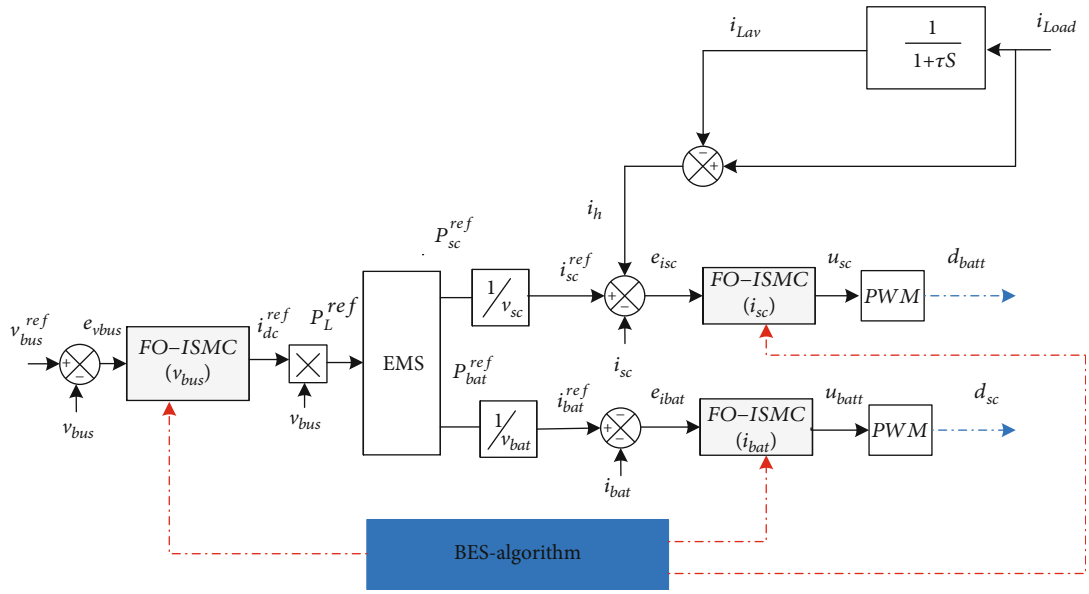

Figure 3: Comprehensive energy maximization strategy schemes.

control loops include two internal current control loops for i_{sd} and i_{sq}, as well as one external speed control loop. The output of the speed controller generates the quadrature reference current, which is compared to the measured current value. Similarly, a current regulation loop is needed to control the direct current i_{sd}. The outputs of the current controllers are the inputs of a decoupling block, which is responsible for producing the reference voltages v_{sd}^{ref} and v_{sq}^{ref}. By making a transformation from the reference (d-q) to the reference (α, β), it is possible to acquire the two voltages' reference $v_{s\alpha}^{ref}$ and $v_{s\beta}^{ref}$ that are necessary for the space vector modulation (SVM) block [64].

In continuation of our discussion on system control, we can now explore the suggested EMS.

4. Suggested EMS Based on Optimal Fractional Order Integral Sliding Mode Controllers

The proposed EMS architecture is divided into two levels (high and low), as shown in Figure 3. The FO-ISM low-level control layer controls the DC/DC converters to ensure a regulated output DC bus voltage and adequate current values according to the contribution of each source (battery or supercapacitor).

To improve EMS efficiency, the bald eagle search (BES) optimization algorithm is used to find the best values for the FO-ISMC parameters k_{v1}, k_{v2}, β, k_{i1}, k_{i2}, k_{i3}, k_{i4}, δbat, δsc, λ_v, λ_{ibat}, and λ_{isc}.

The bald eagle search is an innovative metaheuristic optimization algorithm that takes inspiration from the hunting techniques of the bald eagle [65]. The bald eagle initial step (selecting space) is to choose the most productive region in terms of available food. During the second phase, the eagle looks for its prey inside the allotted space. After establishing its best possible view location during the second phase, the eagle then uses a series of swooping movements to scope out its optimum hunting grounds in the third phase (swooping).

(i) *Choosing the Space Available*

During this phase, the following equation will be used to produce new positions:

$$p_n(it) = p_b + \sigma r(p_{av} - p(it)), \tag{32}$$

where p_n, p_b, and p_{av} are the freshly produced in the i^{th} iteration, best achieved, and average positions, respectively. it is the iteration number, σ denotes a gain controller [1.5, 2], and r denotes a random variable between 0 and 1.

(ii) *Stage of Search and Exploration in Space*

After settling on the best search space, the algorithm next adjusts where the eagles are located within this space. The evolution of the updated model is as follows:

$$p_n(it) = p(it) + y(it)\,(p(it) - p(it+1)) + x(it)\,(p(it) - p_{av}), \tag{33}$$

where x and y vector variables for the i^{th} position are described as follows:

$$x(it) = \frac{xr(it)}{\max(|xr|)}, y(it) = \frac{yr(it)}{\max(|yr|)},$$
$$xr(it) = r(it) \times \sin(\theta(it)), yr(it) = r(it) \times \cos(\theta(it)),$$
$$\theta(it) = k \times \pi \times \text{rand}\,; r(it) = \theta(it) \times R.\text{rand}, \tag{34}$$

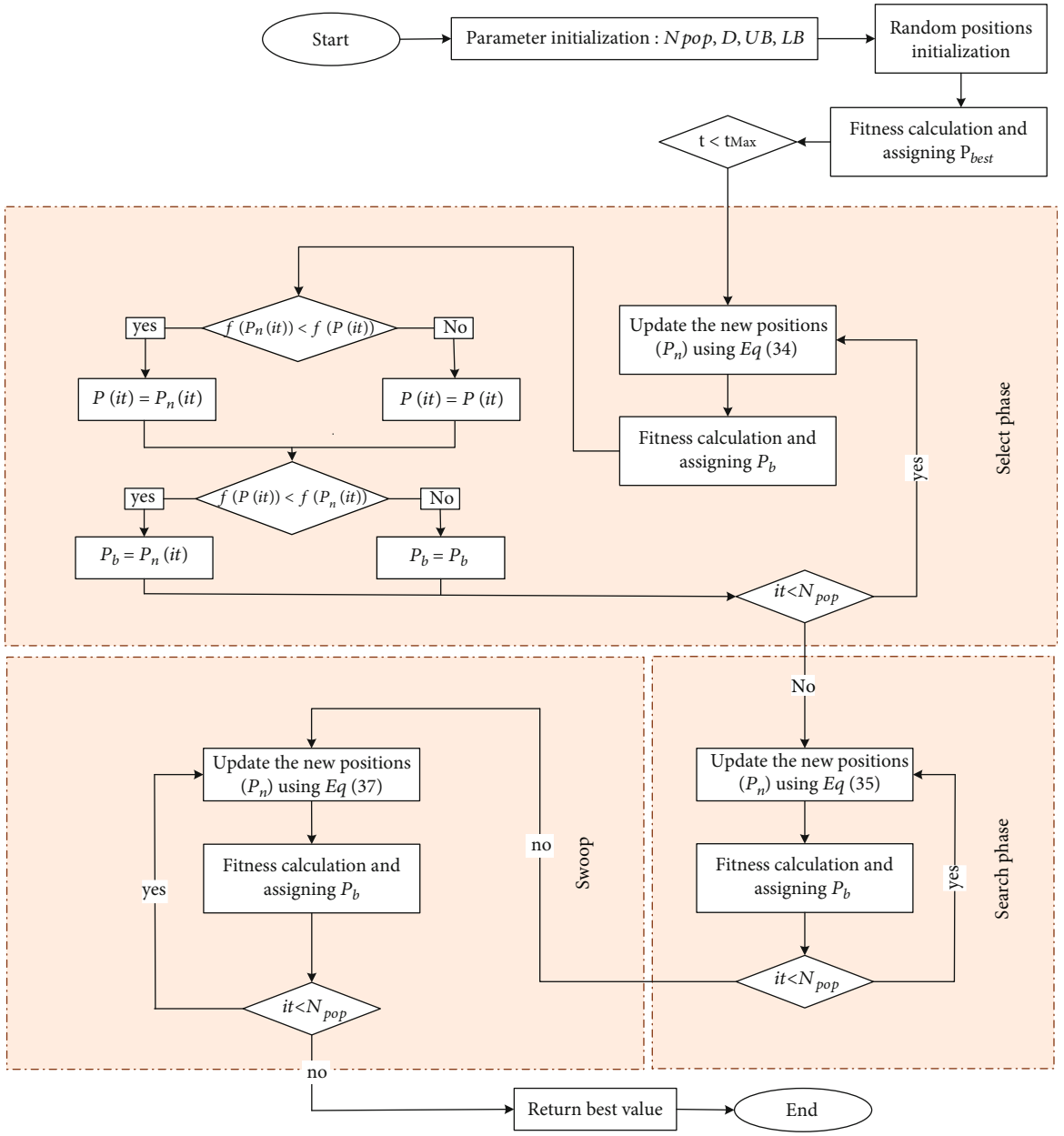

Figure 4: BES flowchart.

where k is a control parameter that takes values in the range [5, 10] and is used to decide the corner between point searches at the center point and R is a parameter that takes values in the range [0.5, 2] and is used to determine the number of search cycles.

(iii) *Stage of Swooping*

At this stage, the eagles begin to swing their bodies from the best position for search towards their prey, as represented in

$$p_n(\text{iter}) = \text{rand} \times p_{\text{b}} + x_1(it) \times (p(it) - c_1 \times p_{\text{av}}) + y_1(it) \times (p(it) - c_2 \times p_{\text{b}}), \tag{35}$$

where c_1 and c_2 are values chosen at random from the range [1, 2] and x_1 and y_1 are directional variables and may be described as

$$x1(it) = \frac{xr(it)}{\max(|xr|)}; y1(it) = \frac{yr(it)}{\max(|yr|)},$$
$$xr(it) = r(it) \times \sinh(\theta(it)); yr(it) = r(it) \times \cosh(\theta(it)),$$
$$\theta(it) = k \times \pi \times \text{rand}; r(it) = \theta(it). \tag{36}$$

Table 1: Optimization parameters.

Parameter	N_{pop}	T_{max}	N_{runs}	D	UB	LB
Value	30	50	10	7	150% of the actual value	50% of the actual value

Npop is the number of populations, *T* max is the maximum of iterations, *D* is the *n*umber of optimization variables, N_{runs} is the number of optimization runs, and *UB* and *LB* are the upper and lower search space limits.

Table 2: Simulation parameters.

Parameters	Value
r_{batt} (Ω)	0.1
r_{sc} (Ω)	0.1
L_{bat} (mH)	2
L_{sc} (mH)	2
V_{bus}^{ref} (V)	400
V_{SC}^{ref} (V)	200
V_{bat}^{ref} (V)	100
c_{SC} (F)	80
c_{bat} (Ah)	450
c_{bus} (μF)	2000

Table 3: Simulation environment.

Simulation environment	Type/value
Software	MATLAB 2021a
Simulation type	Discrete
Sampling size	1*e*-5 s
Simulation time	Start time: 0/stop time: 1400
Solver options	Fixed-step ode4 (Runge-Kutta)

BES optimization algorithm flowchart includes the three optimization stages, selecting space, searching in space, and swooping, as shown in Figure 4.

Following is a flowchart that details all of the optimization steps.

The objective function is as follows:

$$\text{objFun} = \min\left(\int_0^t \sqrt{\varepsilon} dt\right). \tag{37}$$

There are three errors that may be found in hybrid power systems (HPSs), which are as follows:

$$\begin{cases} e_{vbus} = V_{bus}^{ref} - V_{bus}, \\ e_{sc} = \left(i_{sc}^{ref} - i_h\right) - i_{sc}, \\ e_{bat} = i_{bat}^{ref} - i_{bat}. \end{cases} \tag{38}$$

To improve EMS efficiency, the bald eagle search optimization algorithm is used to find the best values for the FO-ISMC parameter set x such that the objective function can be minimized to its minimum value as possible. The following is an example expression the set of parameters to be optimized:

$$x = [k_{v1}, k_{v2}, \beta, k_{i1}, k_{i2}, k_{i3}, k_{i4}, \delta_{bat}, \delta_{SC}, \lambda_v, \lambda_{ibat}, \lambda_{iSC}], \tag{39}$$

with k_{i1}, $k_{i2}k_{i3}$, and k_{i4} and k_{v1} and k_{v2} are the current and voltage coefficients of the FO-ISS; δbat, δsc, and β are the current and voltage fractional orders; and λ_v, $\lambda_{i(bat,sc)}$ are positive constants.

In the first phase, the optimizer places x on the model according to the many potential solutions. After that, an error is produced, and the objective function of each candidate solution x is analyzed. At long last, the optimal solution will be selected to serve as the target solution, a process that will continue right up until the final iteration. The potential solutions need to be constrained within the parameter's restrictions according to the following equation:

$$LB \le x \le UB, \tag{40}$$

where *LB* and *UB* represent the potential solutions' minimum and maximum possible values, respectively.

The BES algorithm parameters are listed in Table 1.

In light of the theoretical framework presented in the previous section, Section 5 focuses on the simulation and cosimulation results to validate our proposed EMS.

5. Results and Discussion

5.1. Simulation Results. In this section, the suggested EMS is validated using MATLAB/Simulink using the UDDS driving cycle and simulation parameters listed in Table 2.

Simulation environment specifications are provided in Table 3.

The speed response of the electric vehicle that is represented in Figure 5 displays good follow-up despite the presence of many changes in the UDDS driving cycle. This confirms the effectiveness of the proposed control system.

Illustration of the torque curve, presented in Figure 6, indicates that the motor generates its maximal torque when the vehicle's speed gets closer to the reference route. After the vehicle has achieved a steady state, the amount of torque generated by the motor will decrease in order to compensate for the torque produced by the load as a whole.

In Figure 7, which depicts the tractive forces of the electric vehicle, it is possible to observe that the acceleration and aerodynamic forces are responsible for a significant portion of the total tractive effort.

As can be shown in Figure 8, the suggested energy management approach can quickly stabilize the DC bus voltage,

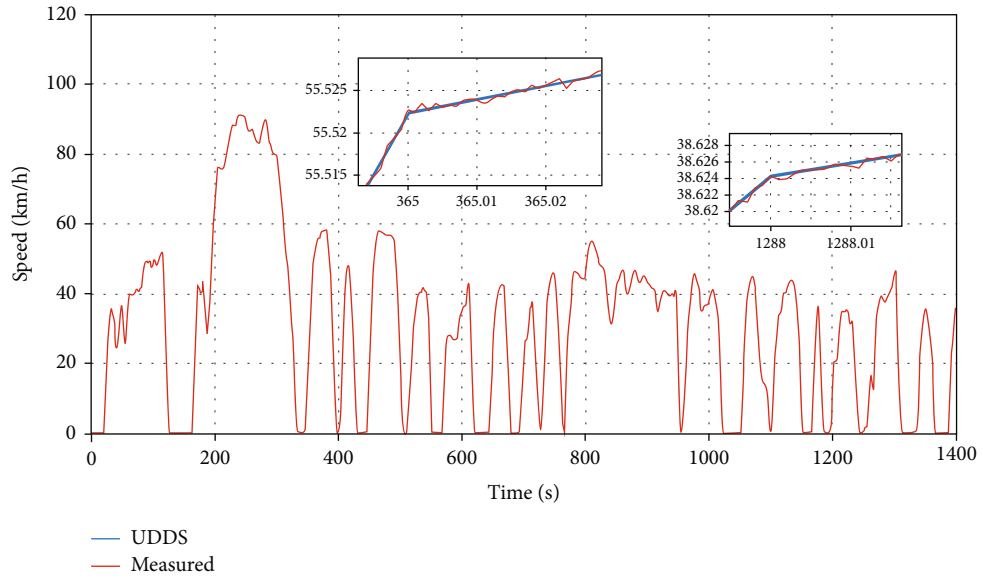

Figure 5: Electrical vehicle linear speed simulation results.

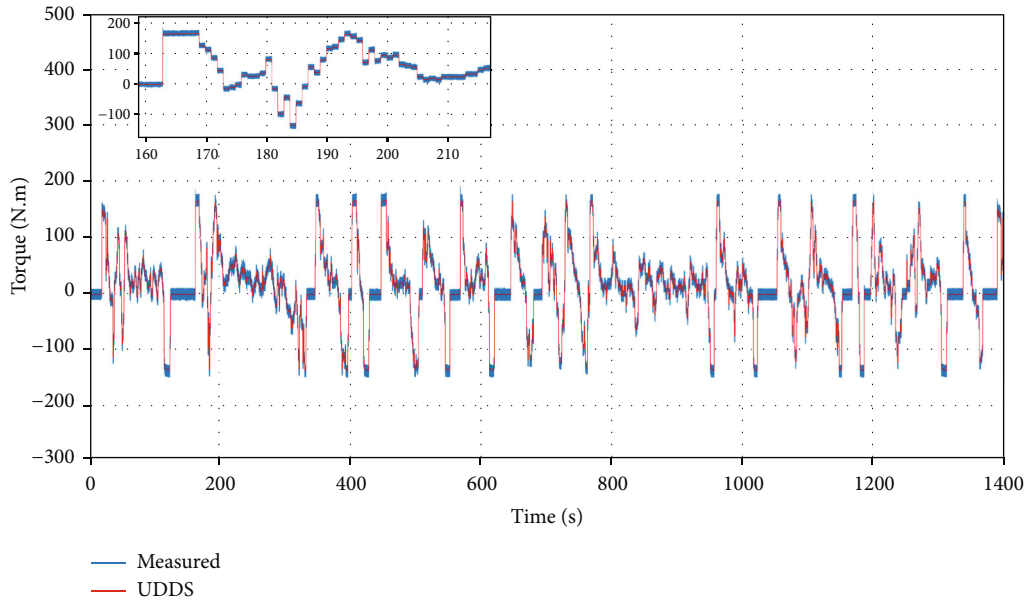

Figure 6: Electrical vehicle load torque (T_L) and synchronous reluctance motor schemes measured torque (T_e).

even when the load power changes significantly. DC bus voltage ripples and voltage overshoots and response time are reduced by the proposed bald eagle search fractional order integral sliding mode control (BES FO-ISMC) EMS compared to that of classical fractional order integral sliding mode control (C FO-ISMC) and fractional order proportional-integral (FO-PI) controller and proportional-integral (PI) controller.

Table 4 presents the findings of a comparison between the BES FO-ISMC proposed EMS and C FO-ISMC and FO-PI controller and PI controller. This table provides an evaluation of the differences in overshoot, as denoted by the equations:

$\Delta V_1 = V_{\text{bus C FO–ISMC OV}} - V_{\text{bus BES FO–ISMC OV}}$, $\Delta V_2 = V_{\text{bus FO–PI OV}} - V_{\text{bus BES FO–ISMC OV}}$, $\Delta V_3 = V_{\text{bus PI OV}} - V_{\text{bus BES FO–ISMC OV}}$, where $V_{\text{bus C FO–ISMC OV}}$ and $V_{\text{bus BES FO–ISMC OV}}$ and $V_{\text{bus FO–PI OV}}$ and $V_{\text{bus PI OV}}$ represent the DC bus voltage overshoots at the instant (t_n) for C F-ISMC and BES-ISMC and FO-PI and PI, respectively.

At high motor loads, such as during acceleration phases, the battery transfers most of its power to the motor, reducing the battery's state of charge (Bat-SOC). As seen in Figure 9, it charges up when the motor torque is negative during deceleration. In the final Bat-SOC, the C FO-SMC and proposed BES FO-SMC are compared in Table 4. The results presented in Table 5 and the Bat-SOC curves in

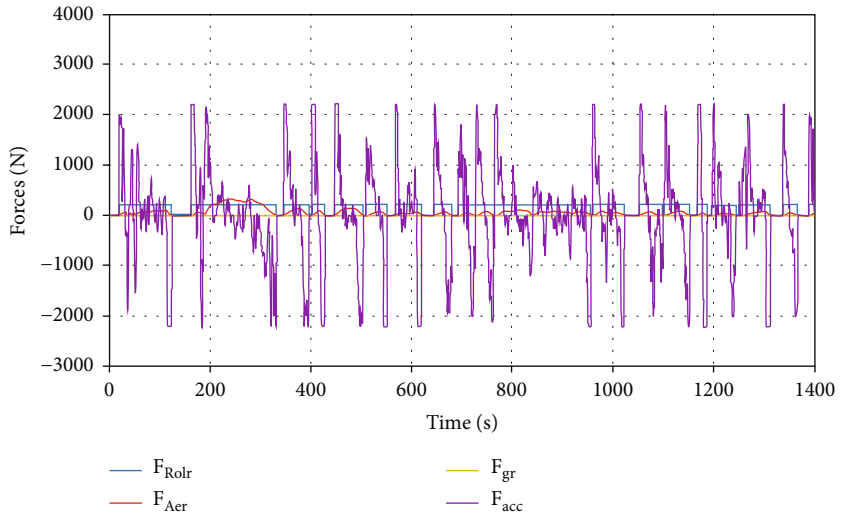

Figure 7: EV tractive forces.

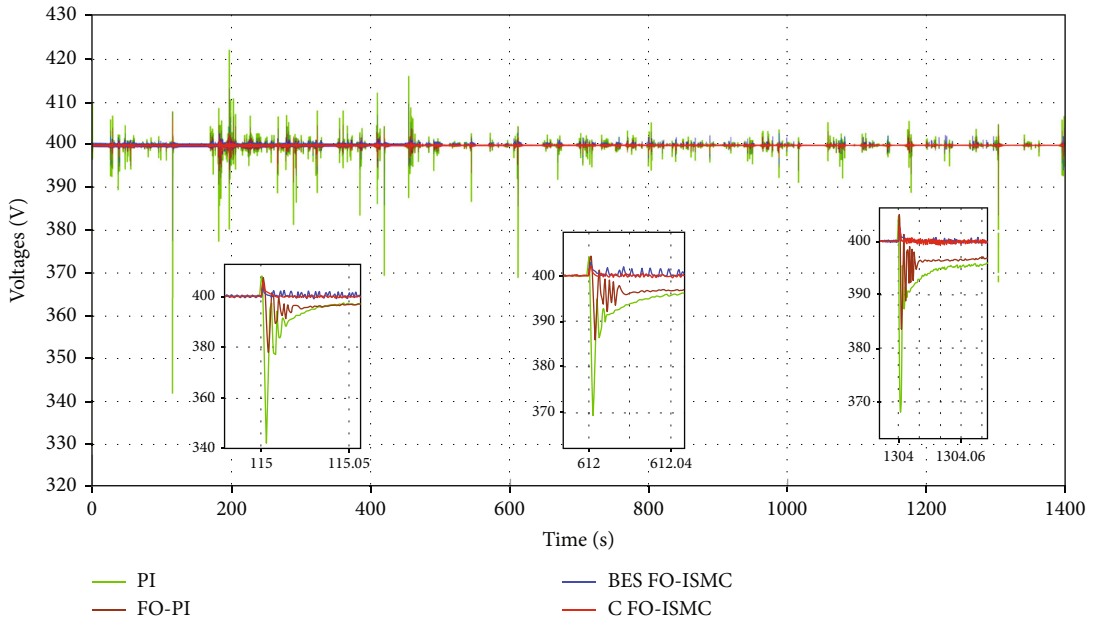

Figure 8: DC bus voltage.

Table 4: Difference in DC bus voltage overshoot.

Time (t_n) (s)	$t_1 = 26$	$t_2 = 186$	$t_3 = 606$	$t_4 = 988$	$t_5 = 1230$	$t_6 = 1269$
EV speed (km/h)	27.2	28.5	36.53	35.41	31	15
$V_{\text{bus C FO–ISMC OV}}$ (V)	2.3	3.5	2.918	7.104	3.5	1.5
$V_{\text{bus BES FO–ISMC OV}}$ (V)	1	1	1.198	2.9	0.7	0.8
$V_{\text{bus FO–PI OV}}$ (V)	5.5	4.5	3	8	4	2
$V_{\text{bus PI OV}}$ (V)	13.16	5	3.6	9	5	3.25
ΔV_1 (V)	1.3	2.5	1.72	4.204	2.8	0.7
ΔV_2 (V)	4.5	3.5	1.8020	5.1	3.3	1.2
ΔV_3 (V)	11.3	4	2.4020	2.2	4.3	2.45
ΔV_1 (%)	0.325	0.625	0.43	1.051	0.7	0.1750
ΔV_2 (%)	1.125	0.875	0.45	1.275	1.0750	0.3
ΔV_3 (%)	2.825	1	0.6	0.55	0.8250	0.6125

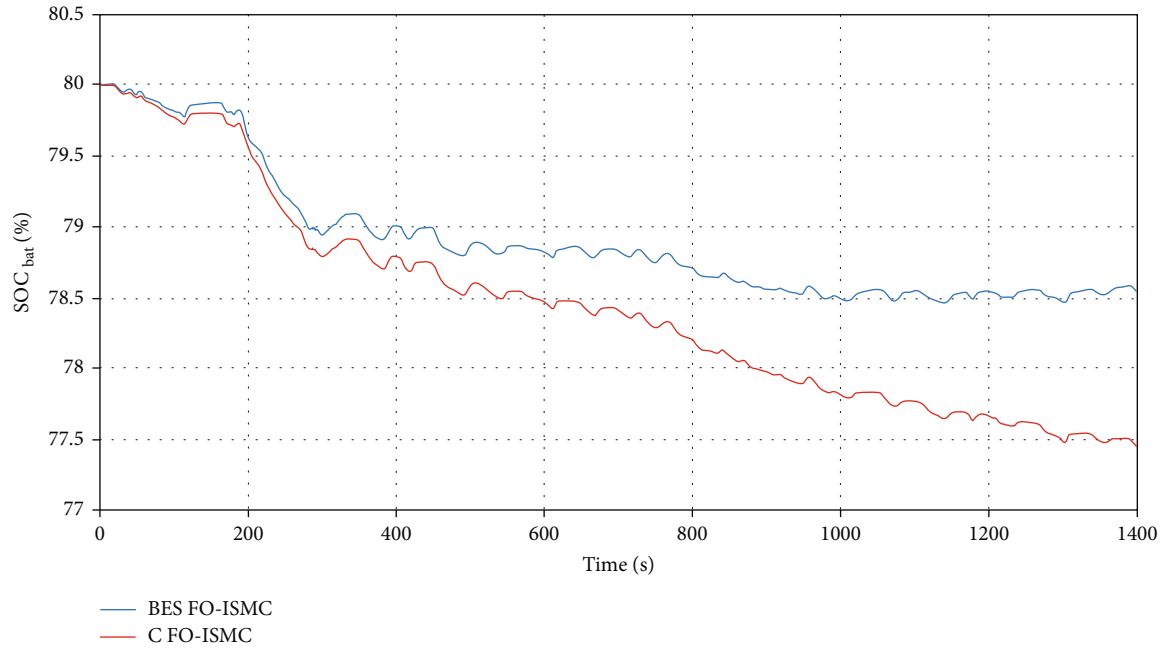

Figure 9: Battery state of charge (%).

Table 5: Difference in the final Bat-SOC.

Cycle drive		UDDS	
EMS	C FO-SMC		BES FO-SMC
Final Bat-SOC (%)	77.44382		78.53973
Diff final Bat-SOC (%)		1.0959	

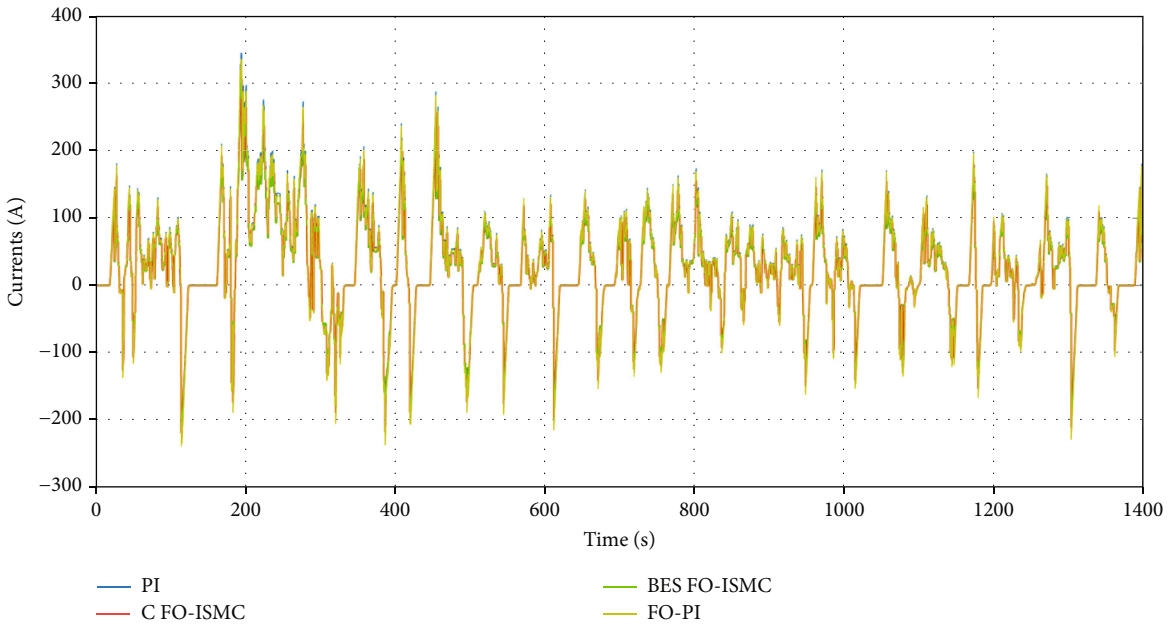

Figure 10: Battery current.

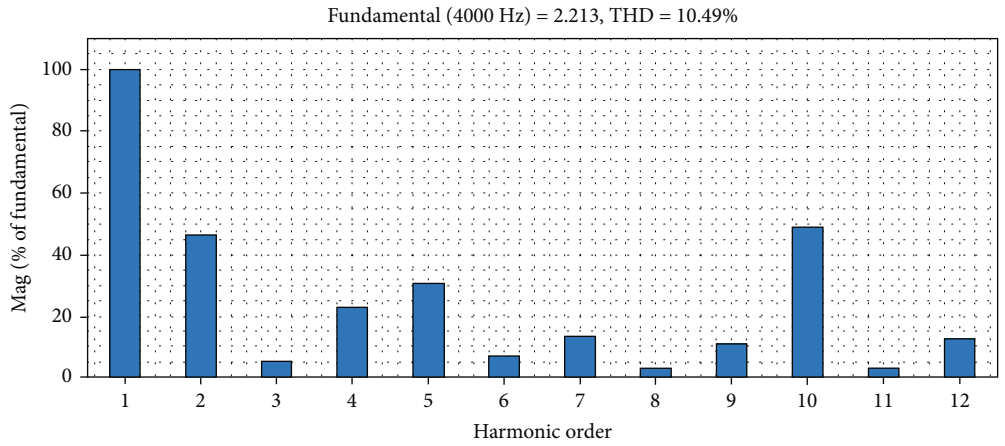

(a)

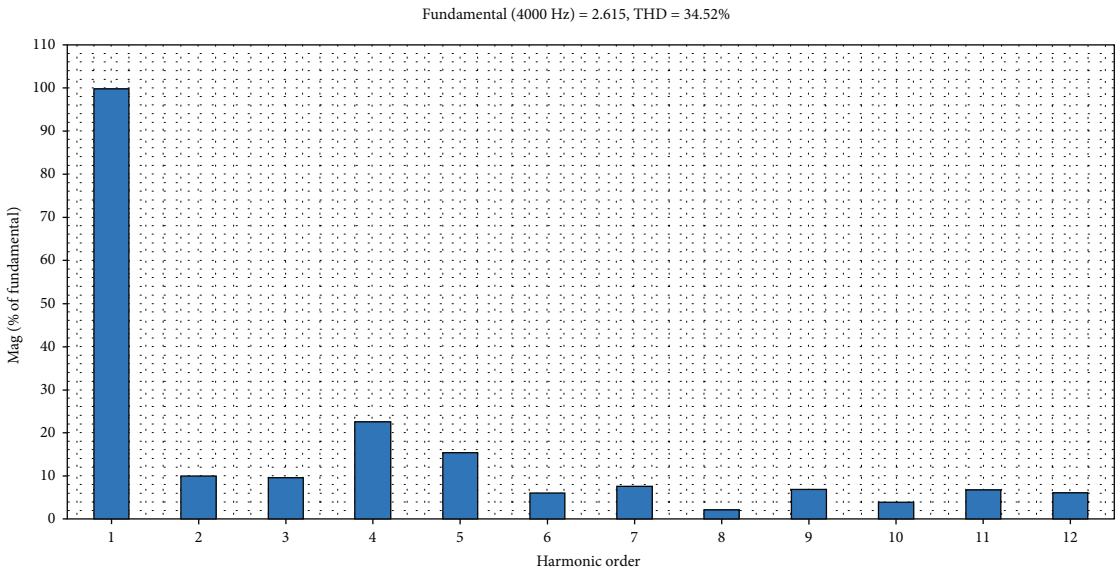

(b)

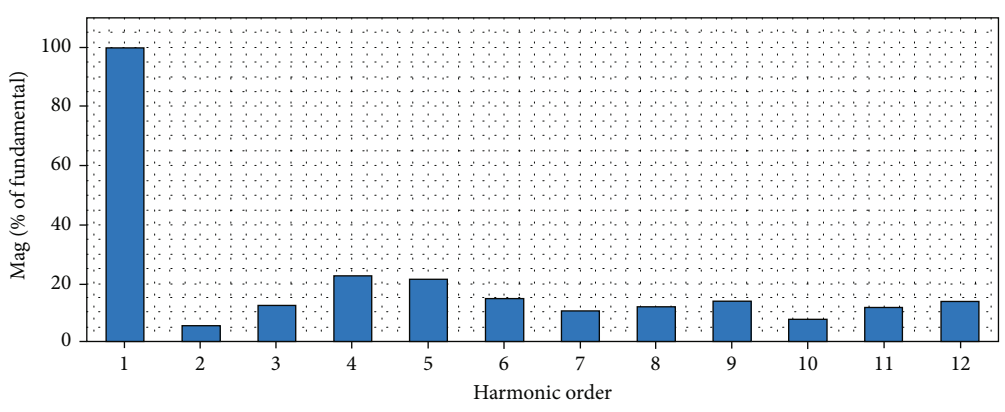

(c)

Figure 11: Continued.

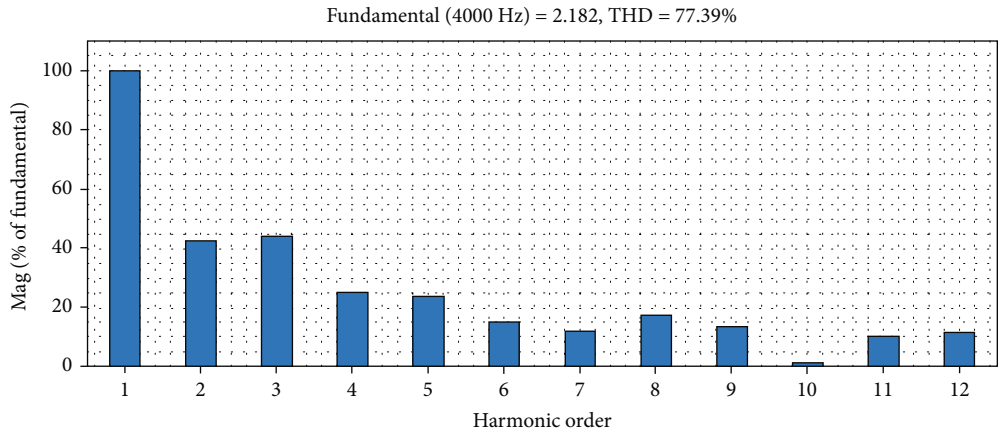

Figure 11: Harmonic spectrum of battery current: (a) for BES FO-ISMC; (b) for FO-PI controller; (c) for PI; (d) for FO-ISMC.

Table 6: Battery current total harmonic distortion.

Cycle drive	UDDS			
EMS	C FO-SMC	BES FO-SMC	FOPI	PI
THD_{ibat} (%)	77.39	10.49	34.52	46.08

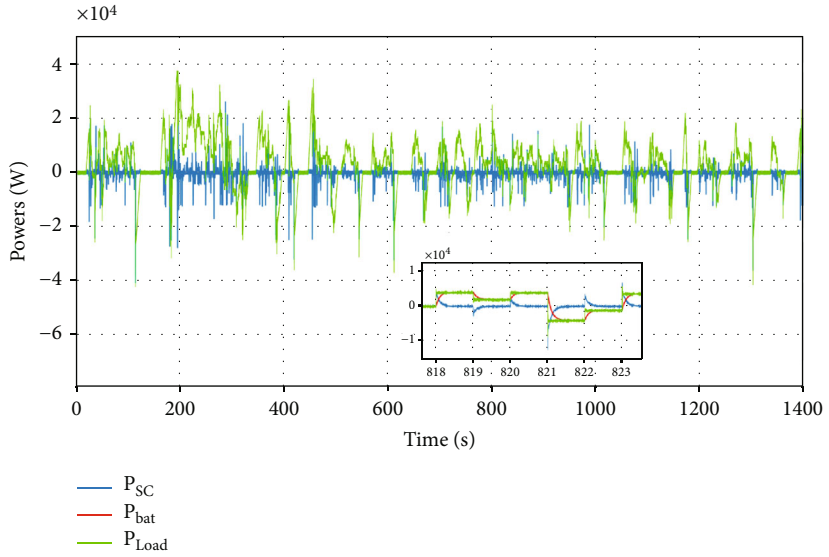

Figure 12: Load, battery, and supercapacitor power waveforms.

Figure 9 demonstrate that the suggested EMS can manage the Bat-SOC more effectively than the classical FO-SMC.

Figures 10 and 11 and Table 6 show that the BES FO-ISMC minimizes the battery current total harmonic distortion (THD_{ibat}) to 10.49% instead of 77.39% for the classical FO-ISMC and 34.52 for the FO-PI strategy and the 46.08 for the PI controller. This finding suits the purpose of the proposed EMS, which is enhancing the battery lifecycle by reducing the battery current harmonics.

According to the power waveforms shown in Figure 12, the battery supplies power to the motor and absorbs it during braking periods. On the other hand, the supercapacitor assists the battery during transient periods, including acceleration and deceleration phases.

Our results shown in Figure 13 confirmed that our EMS effectively manages the energy flows between the sources and the SynRM throughout the UDDS cycle. We achieved similar load, battery, and SC power patterns to those expected under UDDS conditions.

5.2. Cosimulation Part

5.2.1. PIL Implementation Technique Description. The PIL cosimulation technique allows the verification and validation

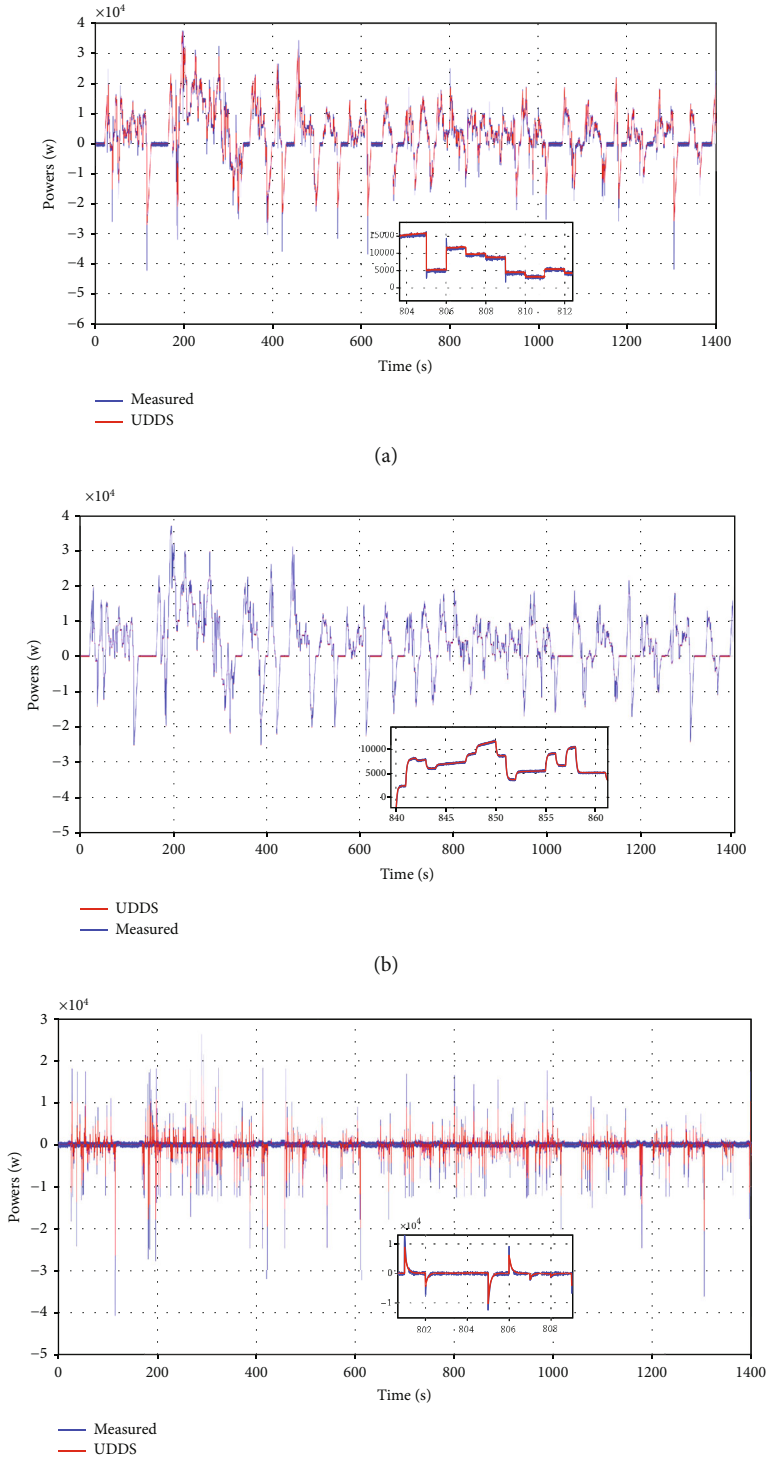

Figure 13: Measured and UDDS reference power waveforms: (a) load power; (b) battery power; (c) supercapacitor power.

of the proposed control algorithms by generating code onto the embedded processor core and running these algorithms in a real environment based on the C2000 launchxl-f28379d DSP board. During PIL cosimulation, the implemented control algorithm is linked to a computer on which the physical system model is carried out. Subsequently, it is possible to evaluate the performance of the system in order to assess and improve some essential factors such as storage capacity, code size, and execution of the algorithm according to the required time. As indicated in Figure 14, during the prototyping of the PIL, based on a fixed simulation time, the power part of the power system is simulated in the

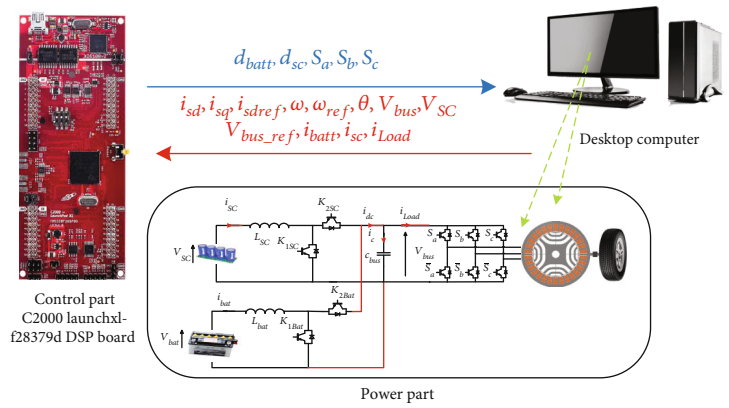

Figure 14: PIL cosimulation strategy scheme.

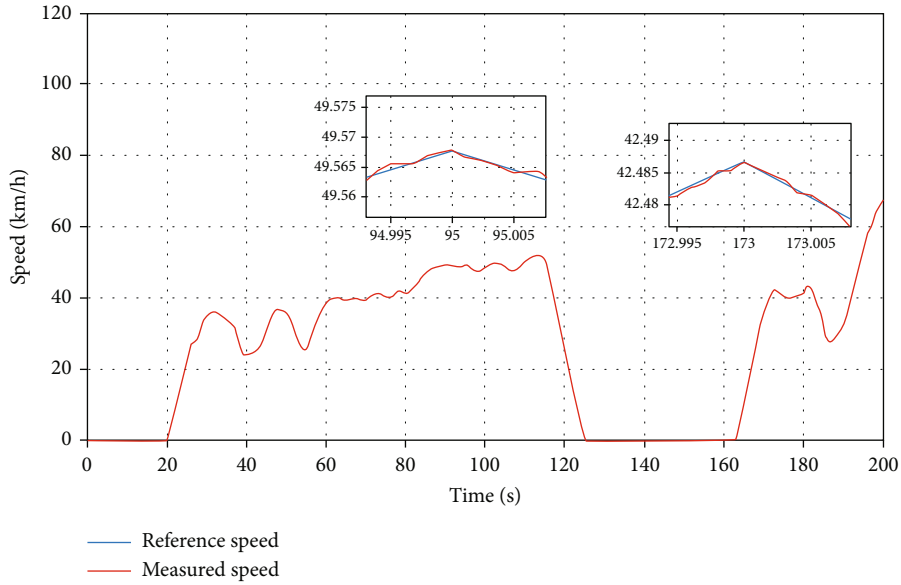

Figure 15: Electrical vehicle linear speed.

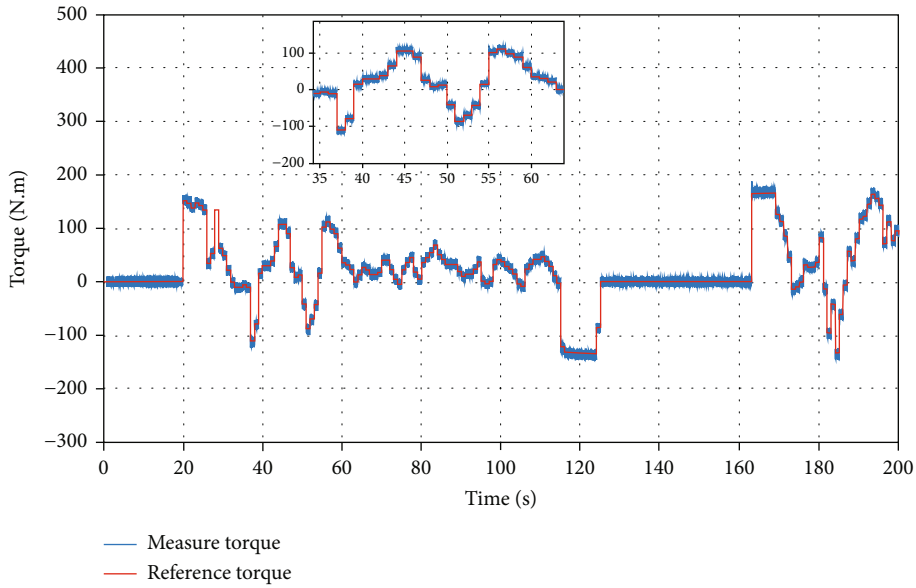

Figure 16: Electrical vehicle load torque (T_L) and synchronous reluctance motor schemes measured torque (T_e).

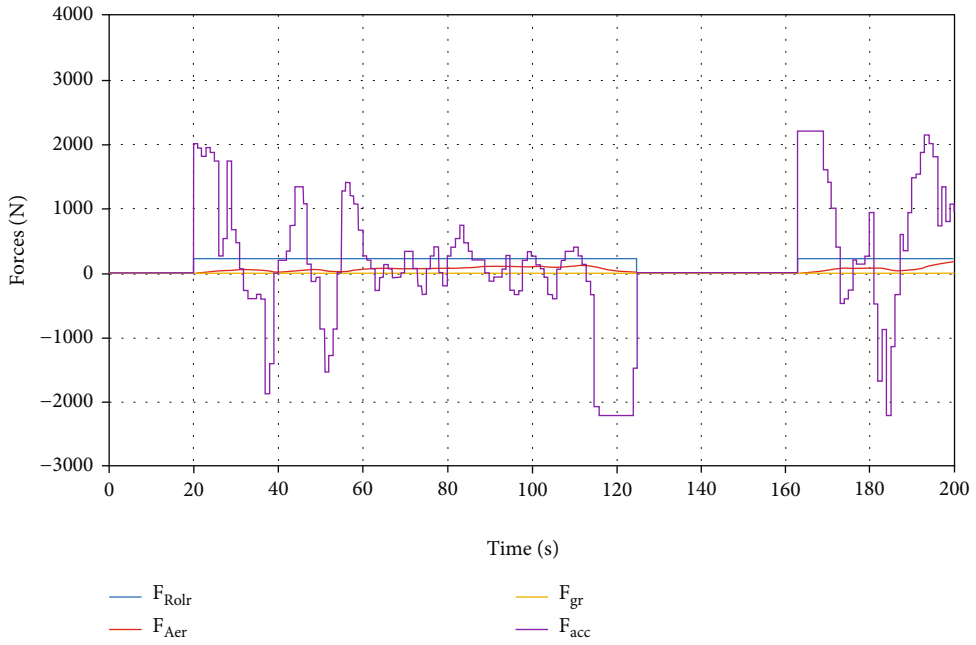

Figure 17: EV tractive forces.

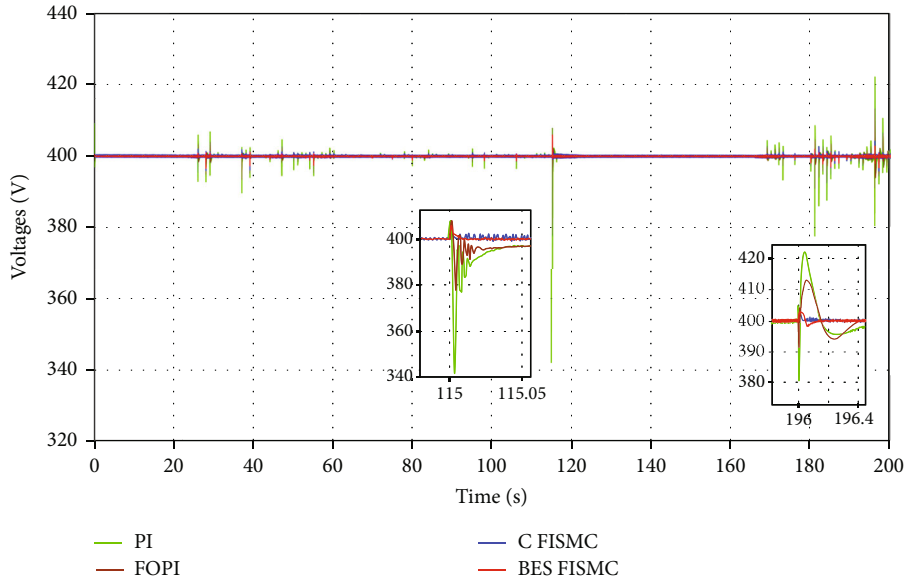

Figure 18: DC bus voltage.

MATLAB/Simulink platform. At each step, the C2000 launchxl-f28379d DSP board receives the signals from the computer, implements control algorithms, and sends the control commands back to the computer to control the power system. At this point, a PIL cosimulation cycle is performed. The data exchange between the computer and the DSP board is synchronized using the serial communication of the DSP board [66].

5.2.2. Cosimulation Results. To approve and evaluate the performance of the suggested EMS, the system was modeled using embedded MATLAB functions and cosimulated using the C2000 launchxl-f28379d DSP board through the processor-in-the-loop. The cosimulation is performed utilizing a reduced-time version of the urban dynamometer driving schedule depicted in Figure 15 based on the parameters listed in Table 1.

The electric vehicle's speed response depicted in Figure 15 demonstrates commendable tracking performance, even in the face of numerous variations within the UDDS driving cycle. This observation serves as validation for the efficacy of the suggested control system.

The depiction of the torque curve, shown in Figure 16, demonstrates that the motor produces its highest torque as

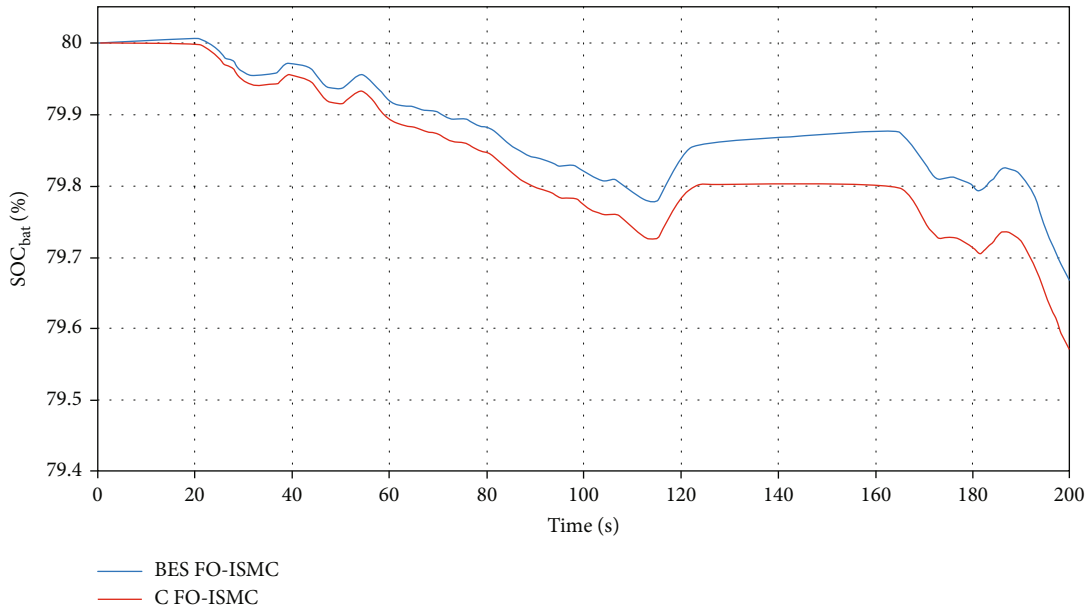

Figure 19: Battery state of charge (%).

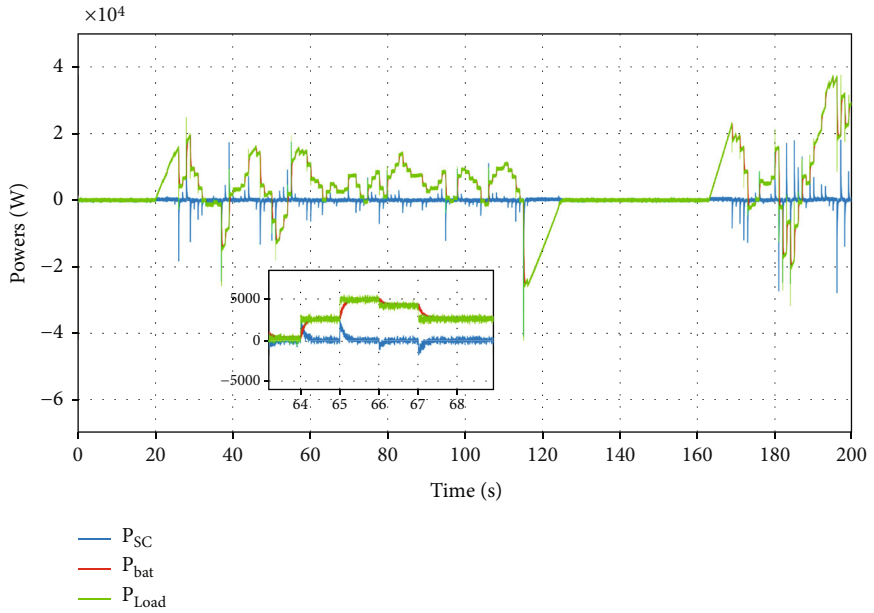

Figure 20: Load, battery, and supercapacitor power waveforms.

the vehicle's speed approaches the reference route. Once the vehicle reaches a stable state, the motor's torque output decreases to counterbalance the overall load-induced torque.

From Figure 17, illustrating the tractive forces of the electric vehicle, it becomes evident that a substantial portion of the overall tractive effort can attribute to the acceleration and aerodynamic forces.

As depicted in Figure 18, the proposed energy management strategy demonstrates its ability to rapidly stabilize the DC bus voltage, even amidst substantial variations in load power. The introduced BES FO-ISMC EMS effectively mitigates DC bus voltage fluctuations, voltage overshoots, and response time, showcasing superior performance in comparison to both the conventional FO-ISMC (C FO-ISMC), FOPI, and PI controller methods.

The SOC graphs shown in Figure 19 collectively underscore the superior efficacy of the suggested energy management system (EMS) in maintaining the battery's SOC compared to the conventional FO-ISMC approach.

As depicted in Figure 20, the battery furnishes the mean power required by the traction system and acquires energy in the braking stages. The supercapacitor aids the battery in momentary intervals (such as acceleration and deceleration

Table 7: Synchronous reluctance motor parameters.

Parameter	Value
Continuous output power (kW)	45
Peak torque in intermediate mode (N.m)	170
Peak torque in continuous mode (Nm)	300
Rated speed (tr/min)	3300
Base speed (tr/min)	1700
Rated current (A)	64.40
Resistance of the stator windings R (Ω)	0.3256
Number of pole pairs p	2
d-axis inductance L_d (mH)	73.2
q-axis inductance L_q (mH)	7.3

Table 8: Vehicle parameters.

Parameter	Value
Mass of vehicle m_v (kg)	1150
Transmission ratio i	10
Aerodynamic drag coefficient C_d	0.32
Tire rolling resistance coefficient μ	0.015
Rotational inertia k_m	1.1
Vehicle frontal area A_f (m^2)	2.5
Air density ξ (kg/m^3)	1.28
Wheel radius r (m)	0.33
Earth gravity g (m/s^2)	9.81

Table 9: Characteristics of Li-ion battery KOKAM 40HED cell.

Parameter	Value
Nominal voltage (V)	3.7
Capacity (Ah)	40
Specific Energy (WA)	133.8
Max current charge/discharge (A)	40/40
Volume (l)	0.42
Weight (kg)	0.935

Table 10: Characteristics of Maxwell technology 350/2.7 supercapacitor cell [19].

Parameter	Value
Nominal voltage (V)	2.7
Capacity (F)	350
Power density (Wh/kg)	4300
Energy (Wh)	5.062
Volume (l)	0.053
Weight (kg)	0.063

phases), aligning with the chosen energy management approach. These findings validate the effectiveness of the proposed EMS in effectively handling both energy storage mechanisms.

6. Conclusion

This research presented a new optimal energy management technique for an electric vehicle's battery/supercapacitor hybrid power system. The proposed management system is based on the optimum fractional order integral sliding mode control and is aimed at efficiently managing the power from both sources in line with the load demand. The fundamental goal of this energy management is to enhance the power quality by maximizing the battery SOC and decreasing the DC bus voltage ripples and voltage overshoots, which have a beneficial impact on the battery lifecycle. In addition, the online updating technique improves the system stability and effectiveness by enhancing its reaction to unforeseen load changes. The obtained simulation and cosimulation results demonstrate the effectiveness of the proposed energy management approach. Concerning the power quality, the proposed energy management system has the ability to reduce the harmonics (THD = 10.49) and attenuate the voltage overshot by ($\Delta V = 1.051$). Concerning the battery usage, the proposed energy management strategy enhanced the battery SoC by 1.0959% at the end of the driving cycle.

In our upcoming studies, we will conduct comparative study to evaluate the performance of BES and other metaheuristics when they are applied to FO-ISMC parameter tuning. This effort is aimed at identifying the strengths and weaknesses of various algorithms for this specific task, considering both convergence speed and complexity.

Appendix

Table 7 provides the parameters for a synchronous reluctance motor (SynRM), and Table 8 contains parameters related to a vehicle. Tables 9 and 10 provide battery and supercapacitor specifications.

These parameters are essential for understanding and analyzing the performance of the synchronous reluctance motor and its application in a specific vehicle setup. They play a crucial role in various engineering calculations and simulations related to motor control, power transmission, and vehicle dynamics.

The KOKAM cells (40HED) are chosen in our case to compose the battery pack, and the Maxwell technology 350/2.7 is chosen due to its very high power, lower weight, volume, and lifetime.

Data Availability

The data is available upon request.

Conflicts of Interest

The authors declare that they have no conflicts of interest.

References

[1] Z. Yao, Y. Wang, B. Liu, B. Zhao, and Y. Jiang, "Fuel consumption and transportation emissions evaluation of mixed traffic flow with connected automated vehicles and human-driven vehicles on expressway," *Energy*, vol. 230, p. 120766, 2021.

[2] M. Groll, "Can climate change be avoided? Vision of a hydrogen-electricity energy economy," *Energy*, vol. 264, article 126029, 2023.

[3] F. Ülengin, M. Işık, Ş. Ö. Ekici, Ö. Özaydın, Ö. Kabak, and Y. İ. Topçu, "Policy developments for the reduction of climate change impacts by the transportation sector," *Transport Policy*, vol. 61, pp. 36–50, 2018.

[4] "Greenhouse gas emissions from transport in Europe — European Environment Agency," n. d. https://www.eea.europa.eu/data-and-maps/indicators/transport-emissions-of-greenhouse-gases/transport-emissions-of-greenhouse-gases-12 (accessed December 8, 2022).

[5] H. Heinrichs, P. Jochem, and W. Fichtner, "Including road transport in the EU ETS (European Emissions Trading System): a model-based analysis of the German electricity and transport sector," *Energy*, vol. 69, pp. 708–720, 2014.

[6] G. Rajendran, C. A. Vaithilingam, N. Misron, K. Naidu, and M. R. Ahmed, "A comprehensive review on system architecture and international standards for electric vehicle charging stations," *Journal of Energy Storage*, vol. 42, article 103099, 2021.

[7] X. Lü, Y. Wu, J. Lian et al., "Energy management of hybrid electric vehicles: a review of energy optimization of fuel cell hybrid power system based on genetic algorithm," *Energy Conversion and Management*, vol. 205, p. 112474, 2020.

[8] I. S. Sorlei, N. Bizon, P. Thounthong et al., "Fuel cell electric vehicles—a brief review of current topologies and energy management strategies," *Energy*, vol. 14, no. 1, p. 252, 2021.

[9] A. Djerioui, A. Houari, S. Zeghlache, and G. Wolf, "Energy management strategy of supercapacitor/fuel cell energy storage devices for vehicle applications," *International Journal of Hydrogen Energy*, vol. 44, no. 41, pp. 23416–23428, 2019.

[10] Z. Zou, J. Cao, B. Cao, and W. Chen, "Evaluation strategy of regenerative braking energy for supercapacitor vehicle," *ISA Transactions*, vol. 55, pp. 234–240, 2015.

[11] G. V. Kumar, C. H. Chuang, M. Z. Lu, and C. M. Liaw, "Development of an electric vehicle synchronous reluctance motor drive," *IEEE Transactions on Vehicular Technology*, vol. 69, no. 5, pp. 5012–5024, 2020.

[12] S. Taghavi and P. Pillay, "A sizing methodology of the synchronous reluctance motor for traction applications," *IEEE Journal of Emerging and Selected Topics in Power Electronics*, vol. 2, no. 2, pp. 329–340, 2014.

[13] D. B. Herrera, E. Galvan, and J. M. Carrasco, "Synchronous reluctance motor design based EV powertrain with inverter integrated with redundant topology," in *IECON 2015 - 41st Annual Conference of the IEEE Industrial Electronics Society*, pp. 3851–3856, Yokohama, Japan, 2015.

[14] Y. H. Kim and J. H. Lee, "Optimum design of ALA-SynRM for direct drive electric valve actuator," *IEEE Transactions on Magnetics*, vol. 53, no. 4, pp. 1–4, 2017.

[15] M. N. F. Ibrahim, E. Rashad, and P. Sergeant, "Performance comparison of conventional synchronous reluctance machines and PM-assisted types with combined star–delta winding," *Energy*, vol. 10, p. 1500, 2017.

[16] C. T. Liu, H. Y. Chung, and S. Y. Lin, "On the electromagnetic steel selections and performance impact assessments of synchronous reluctance motors," *IEEE Transactions on Industry Applications*, vol. 53, no. 3, pp. 2569–2577, 2017.

[17] M. N. Ibrahim, P. Sergeant, and E. M. Rashad, "Synchronous reluctance motor performance based on different electrical steel grades," *IEEE Transactions on Magnetics*, vol. 51, no. 11, pp. 1–4, 2015.

[18] M. M. A. Ansari, W. A. Cronje, and A. Meyer, "Evaluation of a reluctance synchronous motor: for use in an electric mine shuttle vehicle (EMSV)," in *2012 IEEE International Electric Vehicle Conference*, Greenville, SC, USA, 2012.

[19] S. Ferahtia, A. Djeroui, T. Mesbahi et al., "Optimal adaptive gain LQR-based energy management strategy for battery–supercapacitor hybrid power system," *Energies*, vol. 14, no. 6, p. 1660, 2021.

[20] H. Peng, J. Li, L. Löwenstein, and K. Hameyer, "A scalable, causal, adaptive energy management strategy based on optimal control theory for a fuel cell hybrid railway vehicle," *Applied Energy*, vol. 267, p. 114987, 2020.

[21] X. Wang, Y. Huang, F. Guo, and W. Zhao, "Energy management strategy based on dynamic programming considering engine dynamic operating conditions optimization," in *2020 39th Chinese Control Conference (CCC)*, pp. 5485–5492, Shenyang, China, 2020.

[22] Y. Wang, Z. Sun, and Z. Chen, "Development of energy management system based on a rule-based power distribution strategy for hybrid power sources," *Energy*, vol. 175, pp. 1055–1066, 2019.

[23] X. Sun, J. Fu, H. Yang, M. Xie, and J. Liu, "An energy management strategy for plug-in hybrid electric vehicles based on deep learning and improved model predictive control," *Energy*, vol. 269, p. 126772, 2023.

[24] S. Bauer, A. Suchaneck, and L. F. Puente, "Thermal and energy battery management optimization in electric vehicles using Pontryagin's maximum principle," *Journal of Power Sources*, vol. 246, pp. 808–818, 2014.

[25] K. Song, X. Wang, F. Li, M. Sorrentino, and B. Zheng, "Pontryagin's minimum principle-based real-time energy management strategy for fuel cell hybrid electric vehicle considering both fuel economy and power source durability," *Energy*, vol. 205, p. 118064, 2020.

[26] P. Nambisan, S. Member, and M. Khanra, "Optimal energy management of battery supercapacitor aided solar PV powered agricultural feed mill using Pontryagin' s minimum principle," *IEEE Transactions on Power Electronics*, vol. 37, pp. 2216–2225, 2021.

[27] T. L. F. V. P. Tona, "Stochastic dynamic programming based energy management of HEV' s: an experimental validation," *IFAC Proceedings Volumes*, vol. 47, 2014.

[28] S. Zhang and R. Xiong, "Adaptive energy management of a plug-in hybrid electric vehicle based on driving pattern recognition and dynamic programming," *Applied Energy*, vol. 155, pp. 68–78, 2015.

[29] X. Lü, S. Li, X. H. He et al., "Hybrid electric vehicles: a review of energy management strategies based on model predictive control," *Journal of Energy Storage*, vol. 56, article 106112, 2022.

[30] H. Borhan, A. Vahidi, A. M. Phillips, M. L. Kuang, I. V. Kolmanovsky, and S. Di Cairano, "*MPC-based energy management of a power-split hybrid electric vehicle*," *IEEE Transactions on Control Systems Technology*, vol. 20, no. 3, pp. 593–603, 2012.

[31] Z. Lei, D. Qin, L. Hou, J. Peng, Y. Liu, and Z. Chen, "An adaptive equivalent consumption minimization strategy for plug-in hybrid electric vehicles based on traffic information," *Energy*, vol. 190, p. 116409, 2020.

[32] M. Dhifli, A. Lashab, J. M. Guerrero, A. Abusorrah, Y. A. al-Turki, and A. Cherif, "Enhanced Intelligent Energy Management System for a Renewable Energy-Based AC Microgrid," *Energies*, vol. 13, no. 12, p. 3268, 2020.

[33] Y. Zou, T. Liu, D. Liu, and F. Sun, "Reinforcement learning-based real-time energy management for a hybrid tracked vehicle," *Applied Energy*, vol. 171, pp. 372–382, 2016.

[34] Y. Ye, J. Zhang, S. Pilla, A. M. Rao, and B. Xu, "Application of a new type of lithium-sulfur battery and reinforcement learning in plug-in hybrid electric vehicle energy management," *Journal of Energy Storage*, vol. 59, article 106546, 2023.

[35] P. Balakumar, T. Vinopraba, and K. Chandrasekaran, "Deep learning based real time demand side management controller for smart building integrated with renewable energy and energy storage system," *Journal of Energy Storage*, vol. 58, article 106412, 2023.

[36] W. Li, H. Cui, T. Nemeth et al., "Deep reinforcement learning-based energy management of hybrid battery systems in electric vehicles," *Journal of Energy Storage*, vol. 36, p. 102355, 2021.

[37] C. Qi, C. Song, F. Xiao, and S. Song, "Generalization ability of hybrid electric vehicle energy management strategy based on reinforcement learning method," *Energy*, vol. 250, p. 123826, 2022.

[38] Y. Liu, Y. Wu, X. Wang, L. Li, Y. Zhang, and Z. Chen, "Energy management for hybrid electric vehicles based on imitation reinforcement learning," *Energy*, vol. 263, p. 125890, 2023.

[39] L. Han, K. Yang, T. Ma, N. Yang, H. Liu, and L. Guo, "Battery life constrained real-time energy management strategy for hybrid electric vehicles based on reinforcement learning," *Energy*, vol. 259, article 124986, 2022.

[40] G. Du, Y. Zou, X. Zhang, L. Guo, and N. Guo, "Energy management for a hybrid electric vehicle based on prioritized deep reinforcement learning framework," *Energy*, vol. 241, article 122523, 2022.

[41] C. Wu, J. Ruan, H. Cui, B. Zhang, T. Li, and K. Zhang, "The application of machine learning based energy management strategy in multi-mode plug-in hybrid electric vehicle, part I: twin delayed deep deterministic policy gradient algorithm design for hybrid mode," *Energy*, vol. 262, article 125084, 2023.

[42] K. M. S. Y. Konara, M. Kolhe, and A. Sharma, "Power flow management controller within a grid connected photovoltaic based active generator as a finite state machine using hierarchical approach with droop characteristics," *Renewable Energy*, vol. 155, pp. 1021–1031, 2020.

[43] A. U. Rahman, S. S. Zehra, I. Ahmad, and H. Armghan, "Fuzzy supertwisting sliding mode-based energy management and control of hybrid energy storage system in electric vehicle considering fuel economy," *Journal of Energy Storage*, vol. 37, article 102468, 2021.

[44] C. Pan, Y. Tao, Q. Liu et al., "Grey wolf fuzzy optimal energy management for electric vehicles based on driving condition prediction," *Journal of Energy Storage*, vol. 44, article 103398, 2021.

[45] N. Mukherjee and D. Strickland, "Control of cascaded DC-DC converter-based hybrid battery energy storage systems-part I: stability issue," *IEEE Transactions on Industrial Electronics*, vol. 63, pp. 2340–2349, 2015.

[46] F. Yang, B. Sheng, and Y. Fu, "Energy management for fuel cell-supercapacitor hybrid system using passivity-based controller with multi-equilibrium states," in *IECON 2015 - 41st Annual Conference of the IEEE Industrial Electronics Society*, Yokohama, Japan, 2015.

[47] A. Benmouna, M. Becherif, D. Depernet, and M. A. Ebrahim, "Novel energy management technique for hybrid electric vehicle via interconnection and damping assignment passivity based control," *Renewable Energy*, vol. 119, pp. 116–128, 2018.

[48] A. Benmouna, M. Becherif, L. Boulon, C. Dépature, and H. S. Ramadan, "Efficient experimental energy management operating for FC/battery/SC vehicles via hybrid artificial neural networks-passivity based control," *Renewable Energy*, vol. 178, pp. 1291–1302, 2021.

[49] P. Thounthong, P. Tricoli, and B. Davat, "Performance investigation of linear and nonlinear controls for a fuel cell/supercapacitor hybrid power plant," *International Journal of Electrical Power & Energy Systems*, vol. 54, pp. 454–464, 2014.

[50] P. Thounthong, S. Sikkabut, P. Mungporn et al., "Performance investigation of high-energy high-power densities storage devices by li-ion battery and supercapacitor for fuel cell/photovoltaic hybrid power plant for autonomous system applications," in *2015 IEEE Industry Applications Society Annual Meeting*, Addison, TX, USA, 2015.

[51] Z. E. Huma, M. K. Azeem, I. Ahmad, H. Armghan, S. Ahmed, and H. M. M. Adil, "Robust integral backstepping controller for energy management in plugin hybrid electric vehicles," *Journal of Energy Storage*, vol. 42, article 103079, 2021.

[52] K. Sankar and A. K. Jana, "Nonlinear multivariable sliding mode control of a reversible PEM fuel cell integrated system," *Energy Conversion and Management*, vol. 171, pp. 541–565, 2018.

[53] Z. Song, J. Hou, H. Hofmann, J. Li, and M. Ouyang, "Sliding-mode and Lyapunov function-based control for battery/supercapacitor hybrid energy storage system used in electric vehicles," *Energy*, vol. 122, pp. 601–612, 2017.

[54] B. Wang, J. Xu, D. Xu, and Z. Yan, "Implementation of an estimator-based adaptive sliding mode control strategy for a boost converter based battery/supercapacitor hybrid energy storage system in electric vehicles," *Energy Conversion and Management*, vol. 151, pp. 562–572, 2017.

[55] B. Yang, Y. Hu, H. Huang, H. Shu, T. Yu, and L. Jiang, "Perturbation estimation based robust state feedback control for grid connected DFIG wind energy conversion system," *International Journal of Hydrogen Energy*, vol. 42, no. 33, pp. 20994–21005, 2017.

[56] B. Yang, T. Yu, H. Shu, J. Dong, and L. Jiang, "Robust sliding-mode control of wind energy conversion systems for optimal power extraction via nonlinear perturbation observers," *Applied Energy*, vol. 210, pp. 711–723, 2018.

[57] P. K. Ray, V. P. Singh, S. R. Mohanty, N. Kishor, and S. Sen, "Frequency control based on H ? controller for small hybrid power system," in *2011 5th International Power Engineering and Optimization Conference*, Shah Alam, Malaysia, 2011.

[58] J. Heidary, M. Gheisarnejad, and M. H. Khooban, "Stability enhancement and energy management of AC-DC microgrid based on active disturbance rejection control," *Electric Power Systems Research*, vol. 217, article 109105, 2023.

[59] S. Safiullah, A. Rahman, and S. A. Lone, "A2ndorder active disturbance rejection controller for coordinated frequency-voltage control of deregulated hybrid power system with

optimal electric-vehicle integration," *Electric Power Systems Research*, vol. 210, article 108129, 2022.

[60] B. Yang, J. Wang, Y. Sang et al., "Applications of supercapacitor energy storage systems in microgrid with distributed generators via passive fractional-order sliding-mode control," *Energy*, vol. 187, article 115905, 2019.

[61] B. Yang, J. Wang, X. Zhang et al., "Applications of battery/supercapacitor hybrid energy storage systems for electric vehicles using perturbation observer based robust control," *Journal of Power Sources*, vol. 448, article 227444, 2020.

[62] C. Monje, Y. Q. Chen, B. M. Vinagre, D. Xue, and V. Feliu, *Fractional-order systems and controls: fundamentals and applications*, Springer Science & Business Media, 2010.

[63] M. P. Aghababa, "A Lyapunov-based control scheme for robust stabilization of fractional chaotic systems," *Nonlinear Dynamics*, vol. 78, no. 3, pp. 2129–2140, 2014.

[64] G. H. Eddine, B. Said, A. Houari, A. Dieroui, and T. Mesbahi, "Integral sliding mode control of synchronous reluctance machine based electric vehicle powered by battery/supercapacitor hybrid source," in *2022 19th International Multi-Conference on Systems, Signals & Devices (SSD)*, Sétif, Algeria, 2022.

[65] H. A. Alsattar, A. A. Zaidan, and B. B. Zaidan, "Novel meta-heuristic bald eagle search optimisation algorithm," *Artificial Intelligence Review*, vol. 53, no. 3, pp. 2237–2264, 2020.

[66] H. E. Ghadbane, S. Barkat, A. Houari, A. Djerioui, and T. Mesbahi, "Energy Management Strategy for Hybrid Power System Implemented with Processor in the Loop," in *2022 IEEE International Conference on Electrical Sciences and Technologies in Maghreb (CISTEM)*, Tunis, Tunisia, 2022.